VLÁKNA a TEXTIL

Ročník 12.
2005

ISSN 1335-0617

Indexed in:

Chemical Abstracts,

World Textile Abstracts

EMBASE

Elsevier Biobase

Elsevier GeoAbstracts

Vlákna a Textil (4) 2005
Fibres and Textiles (4) 2005

CONTENTS

OBSAH

THERMOPHYSIOLOGICAL PROPERTIES OF INTEGRATED TEXTILE LAYERS DESIGNED FOR AN EXTREMELY LOW TEMPERATURE ENVIRONMENT

Murárová A.[1], Rusnák A.[1], Murárová Z.[2]

[1]*Slovak University of Technology, Faculty of Chemical and Food Technology, Radlinského 9, 81237 Bratislava, Slovak Republic, E-mail: anna.murarova@stuba.sk*

[2]*Comenius University, Medical Faculty, Špitalská 24, 81372 Bratislava, SK*

The paper deals with the thermophysiological properties of integrated textile layers designed for an extremely low temperatures environment. An integrated model textile layer consists of a lower layer A, an inner layer B+i+B and upper layer C, according to the following scheme A+(B+i+B)+C. We focused on the thermal resistance of the inner thermal-isolating layer i and the thermal-humidity profile of the lower textile layer A. We designed an integrated textile layer with a suitable thickness for the thermal-isolating layer i from a non-woven PET textile which would assure the thermal isolation of a body during minimal physical effort and a minimal outside temperature. The thermal-humidity profile of the lower textile layer was monitored using time shrinkage. We evaluated the synergic effect of the textile layer B to the time shrinkage of the textile layer A.

Keywords: Integrated textile layers, thermophysical properties, thermal resistance, thermal-humidity profile

INTRODUCTION

When considering an evaluation of thermophysical comfort during the wearing of clothes designed for different conditions (extremely low temperatures, high physical effort, clothes for a clean environment, etc.), it is important to evaluate the composition of the specific textile layers as well as the composition of the integrated textile layers. An integrated textile layer composed of simple layers and its thermophysical properties are determined by the arrangement of the specific textile layers. The correct composition of a textile layer in integrated layers (lower, inner, upper) will assure their transport properties. An incorrect composition of a textile layer can cause physiological discomfort. There is a great deal of progress currently being made in the research on textile material designed for clothing. Due to the scientific approach used during evaluation of the interaction between a textile material, the physiological functions of skin and the outside climate conditions, a textile material can fulfill strict criteria for thermophysiological comfort during different physical activities [1–10].

The correct composition of specific textile layers is very important during the design of integrated textile layers for special clothing especially in cases where specific textile layers are mutually fixed without the option of change. Every specific textile layer is individual and has specific properties and a specific macromorphological structure. It is therefore important to know the functional properties of both the individual and integrated textile layers and the synergism between mutual the contact layers to their thermophysical properties [10–14].

EXPERIMENTAL

Experimental material

Table 1 illustrates the composition of specific textile layers and their arrangement in an integrated textile layer.

Integrated textile layers models are composed of three layers: lower A, inner B+i+B, and upper C. The integrated textile layer models and their composition are stated in Table 3.

Experimental methods

We used a contact laboratory method on an Alambeta machine in order to measure thermal resistance of the areas of the simple and integrated textile layers. This method is based on the principle of heat transfer by conduction during the contact between a heating board and textile surface. The pressure from a heating board to a textile's surface is 200 Pa. The thermal resistance was measured over a difference in temperature of 40 °C. The samples were air-conditioned at a temperature of 23 °C and a relative air humidity of 51%.

The textiles designed for the lower layer A were measured on the Alambeta machine together with surfaces which were watered repeatedly until they were dry at 5-minute time intervals in combination with the B samples. We watered the surface of the A sample. The time of the drying process was identical with the time when the value of the thermal resistance of the area of the textile reached the value of the thermal resistance of the dry sample.

Table 1 The composition of material in integrated textile layers

No.	Material composition of a textile	Kind of textile	Textile arrangement in an integrated layer
1	100% cotton I	Knitting	Lower layer – A
2	40% viscose fibre and 60% polypropylene fibre (40% Vs / 60% PP)	Knitting	Lower layer – A
3	20% cotton and 80% polypropylene fibre I (20% cotton / 80% PP I)	Knitting	Lower layer – A
4	20% cotton and 80% polypropylene fibre II (20% cotton / 80% PP II	Knitting	Lower layer – A
5	100% polypropylene fibre (PP)	Knitting	Lower layer – A
6	60% cotton and 40% polypropylene fibre (60% cotton / 40% PP)	Knitting	Lower layer – A
7	100% cotton II	Knitting	Lower layer – A
8	100% polyester microfibre (PET)	Fabric	Inner layer – B
9	Polyester microfibre and carbon fibre (PET-C)	Fabric	Outside layer – C
10	100% polyester fibre (PET)	Non-woven textile	Inner layer - i

Table 2 Basic properties of textile materials

Kind of textile	Thickness [mm]	Area weight [g.m^{-2}]
100% cotton I	0.79	169
40%Vs / 60% PP	0.71	167
20% cotton/80%PP I	1.50	207
20% cotton/80%PP II	1.80	233
100% PP	0.70	96
60% cotton/40%PP	1.02	181
100% cotton II	0.58	130
100% PET microfibre	0.16	100
PES - C microfibre	0.17	132
PES non-woven textile	2.55	Fibre fineness [dtex] 13.2

RESULTS AND DISCUSSION

The integrated textile layers consisted of a lower layer, inner layer and upper layer according to the following scheme A+(B+i+B)+C. Layer A in the integrated textile layer changed. For the A sample, we used knitting of a different composition made from cotton, polypropylene and viscose fibres in a 100% and a blended composition as well as different macromorphological structure in order to evaluate their thermal-humidity profile. The B layer has fabric made from PET microfibres. The B layer in an integrated textile layer should guarantee the increased transport of humidity from the lower layer A but at the same time, limit the inner air flow during motion in the thermo-isolating layer i from the non-woven textile. The inner layer of the integrated textile layer is composed of B+i+B. The inside thickness of the inner layer of the isolating layer i changed by superposition (i*1, i*2, i*3, i*4, i*5). The isolating layer i is a non-woven textile made of PET fibres. The Upper layer C is made of fabric from PET microfibres with carbon-conducting fibres. Such a fabric is designed for clothing for clean environments. All kinds of textile materials can be applied to the upper layer of an integrated textile layer according to their usage. From the point of view of modeling integrated textile layers into an extremely low temperature environment, it is very important to consider the inner isolating layer and transport of humidity in a direction from the lower layer to the other layers in order to guarantee a dry underclothing micro-climate and thermal-humidity comfort during physical effort.

Picture 1 illustrates the thermal resistance of all the integrated textile layer models. It demonstrates that the thickness of the isolating layer has the biggest influence on an change in the thermal resistance of an integrated textile layer. During the superposition of 4*i and 5*i, you can observe the non-linearity of thermal resistance from the number of i layers, which is related to the deformability of an integrated textile layer during pressure from s heating board as well as the technical possibilities of a measuring machine to measure thermal resistance. The influence of A layer on the thermal resistance of an integrated textile layer is less important in comparison with the change in thickness of thermo-isolating layer i.

Based on the measured thermal resistances of the integrated textile layer models, we calculated the minimal temperature of a climate during which the thermal isolation of a human body would still be sufficient. We used the following equation to calculate minimal temperature of climate T_{amin}:

$$H = [(T_s - T_{a\,min}) \times a]/r$$

where H = 44 W is the heat output of a human body during minimal physical effort, T_s = 35 °C the medium temperature of the skin surface, $T_{a\,min}$ [°C] the minimal temperature of the climate, a = 1,68 m^2 for the skin surface of an adult, r [m^2.°C.W^{-1}] the area resistance of the heat transfer through an integrated textile layer.

Table 3 Integrated textile layers

Integrated layer	A							B	C	i Number of layer layelayerslaye lalayers				
	100 % cotton I	40%/60% Vs/PP	20%/80% cotton/PP I	20%/80% cotton/PP II	100% PP	60%/40% cotton / PP	100 % cotton II	100% PET	PET+Carbon	1	2	3	4	5
A+B+1i+B+C	+							+	+	+				
A+B+2i+B+C	+							+	+		+			
A+B+3i+B+C	+							+	+			+		
A+B+4i+B+C	+							+	+				+	
A+B+5i+B+C	+							+	+					+
A+B+1i+B+C		+						+	+	+				
A+B+2i+B+C		+						+	+		+			
A+B+3i+B+C		+						+	+			+		
A+B+4i+B+C		+						+	+				+	
A+B+5i+B+C		+						+	+					+
A+B+1i+B+C			+					+	+	+				
A+B+2i+B+C			+					+	+		+			
A+B+3i+B+C			+					+	+			+		
A+B+4i+B+C			+					+	+				+	
A+B+5i+B+C			+					+	+					+
A+B+1i+B+C				+				+	+	+				
A+B+2i+B+C				+				+	+		+			
A+B+3i+B+C				+				+	+			+		
A+B+4i+B+C				+				+	+				+	
A+B+5i+B+C				+				+	+					+
A+B+1i+B+C					+			+	+	+				
A+B+2i+B+C					+			+	+		+			
A+B+3i+B+C					+			+	+			+		
A+B+4i+B+C					+			+	+				+	
A+B+5i+B+C					+			+	+					+
A+B+1i+B+C						+		+	+	+				
A+B+2i+B+C						+		+	+		+			
A+B+3i+B+C						+		+	+			+		
A+B+4i+B+C						+		+	+				+	
A+B+5i+B+C						+		+	+					+
A+B+1i+B+C							+	+	+	+				
A+B+2i+B+C							+	+	+		+			
A+B+3i+B+C							+	+	+			+		
A+B+4i+B+C							+	+	+				+	
A+B+5i+B+C							+	+	+					+

Values H, T_s, in the above equation are taken from literature [2].

Picture 2 illustrates the integrated textile layer models that will guarantee the thermal isolation of the human body during low temperatures in an outside climate and during minimal physical effort. According to our research, integrated textile layers which have an inner layer of an non-woven PET textile of a i*4 a i*5 thickness meet the criteria for usage in extremely low temperatures.

From the point of view of a physiological and interactive evaluation of a textile, skin and climate during minimal physical effort and a low outside temperature, no increased sweating occurs, therefore the lower layer of an integrated textile layer which is in contact with skin will not be burdened by the transport of sweat. Indeed, during grater physical effort, heat and sweat output is higher. A higher physical effort induces more moisture through a textile layer. From a thermophysiological point of view and comfort, the

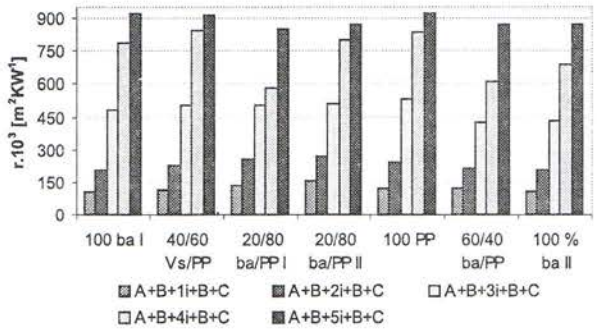

Fig. 1 Thermal resistance of integrated textile layers of various compositions. A – lower layer-hosiery -7 kinds, B – inner layer-fabric from PES micro-fibre-1type, i – isolating inner layer--non-woven PES texile-1 to 5 layers, C – upper barrier layer

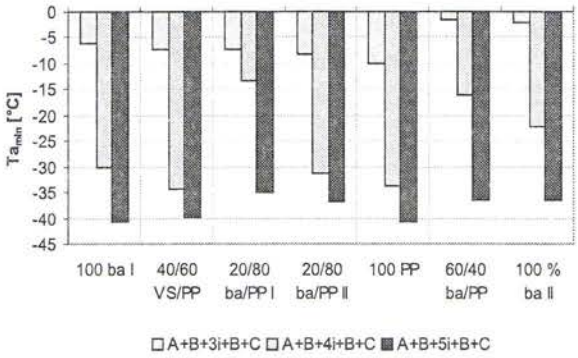

Fig. 2 Minimal environment at temperature designed for various integrated textile layers for a human body at a physical effort of 144 W. A – lower layer-hosiery -7 kinds, B – inner layer-fabric from PES micro-fibre-1type, i – isolating inner layer-non--woven PES textile-1 to 5 layers, C – upper barrier layer.

most important requirement concerns the textile layer which is in contact with skin. That is why we focused on the lower layer and evaluated its thermo-humidity profile. The thermo-humidity profile of the lower layer A was monitored according to the kinetics of the drying of textiles moistened by the same amount of water. The time during which the thermal resistance equaled the dry sample is the drying time. Thermal resistance dramatically changes with the humidity content in a textile. In a dry status, thermal resistance is low, and it raises with a decrease in humidity. A textile reaches its highest thermal resistance in a dry status. Picture 3 illustrates the thermal-humidity profile of 7 kinds of textiles which were used in the lower layer of an integrated textile layer. Table 2 shows the thickness and weight of the area of these textiles. Each textile has a

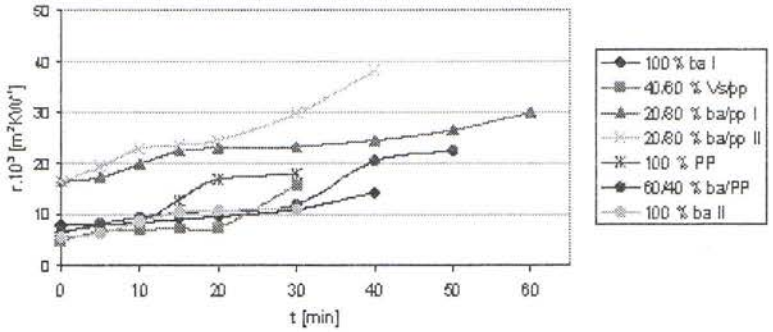

Fig. 3 Thermal humidity profile during the drying of lower textile layers ofvarious compositions

Table 4 Monitoring time the drying time of textile layer A and double-layer A+B

Kind of textile A	r.10³ [m²KW⁻¹] A+B in dry status	Drying time [min] A	Drying time [min] A+B
100% cotton I	14.1	40	35
40%Vs / 60% PP	15.6	30	20
20% cotton/ 80%PP I	32.0	60	40
20% cotton/ 80%PP II	39.1	40	20
100% PP	17.5	30	15
60% cotton/ 40%PP	22.5	50	45
100% cotton II	12.1	30	25

specific chemical composition, macromorphological structure and related transport properties and thermal resistance in its wet and dry statuses.

We discovered an interesting fact during the drying of these samples in combination with a fabric made from PET microfibres (sample B). When talking about the double-layer A+B textile, the textile was moistened on the A side, and we measured the drying time, table 4.

According to the stated time values for the drying of textile double-layer A+B in table 4, we can see the influence of the synergetic effect of textile layer B on the drying time of textile layer A. Textile double-layer A+B has a macromorphological structure composed of fine fibres and microfibres with a different adhesion humidity transport on fibre surfaces as well as a different capillar transport between fine and microfine fibres. The correct layer disposition resulted in transport of moisture from layer A which contained fine fibres, to

layer B, which contained microfibres. Due to the different unit weights, we observed "denier effect" and a synergetic effect shortened drying time. The drying time of the doublelayer textile A+B was monitored using the same procedures as the A layer. The drying time was identical to the time when a stable thermal resistance was reached the corresponded to the thermal resistance of double-layer A+B in a dry status. The drying time of the double-layer A+B composed of 100% PP knitting and 100% PET fabric made from microfibres was shortened by 50%. This double-layer textile had the shortest drying time in set of all the A+B textiles. That is why from a thermophysiological point of view and comfort, the textile made from 100% PP is the most suitable among all the evaluated textiles in the lower layer of an integrated textile layer.

CONCLUSION

- By evaluating the thermal resistance of integrated textile layer models using the contact method during heat transport by conduction and the 200 Pa pressure of a heating board on an integrated textile layer, we determined that textiles with a thermal-isolation layer made from PET of a non-woven textile and a thickness of i*4 and i*5 are suitable to guarantee thermal-isolating protection of the human body during extremely low temperatures and a physical effort of 144 W.
- PES fabric from microfibres – layer B in integrated textile layers has a synergetic effect of the drying time of a double-layer A+B textile based on a different fineness of the fibre in layer A and layer B. At the same time, the transport of humidity was directed from textile layer A with thicker fibres to textile layer B with microfibres. This synergetic effect was mostly demonstrated by the shortening of drying time by 50% of a textile double-layer composed of 100% PP knitting and 100% PES fabric made from microfibres.
- From a thermal-humidity point of view, knitting made from 100% PP fibres is the most suitable textile among the textiles evaluated to be used in the lower layer of an integrated textile layer.

Acknowledgement: The work was supported by the Research VEGA 1/2451/05

REFERENCES

[1] Gimpel S., Umbach K. H.: Integrated protective clothing for low temperature work places. Vlákna a textil 2(3)109–113,1995
[2] Murárová A.: Physiology of Clothing I. Men's Thermal Regulation. Vlákna a textil 8(1) 48–49, 2001
[3] Murárová A.: Physiology of Clothing II. Apparel as a Physiological System. Vlákna a textil 8 (1) 50–52, 2001
[4] Murárová A., Jambrich M., Murárová Z.: Physiology of Clothing III. Comfort. Vlákna a textil 8 (4) 279–283, 2001
[5] Murárová, A.: Physiology of Clothing IV. Humans and Hygienic Properties. Vlákna a textil 8 (4) 284–286, 2001
[6] Murárová A., Jambrich M., Balogová A.: The influence of the composition of textile materials on their physiological properties. Vlákna a textil 11(1)3–12, 2004
[7] http://howthingswork.virginia.edu/supplements/clothing_and_insulation.pdf
[8] Hes L., Balcaříková V.: Objective evaluation of the thermal efficiency of protective garments containing PCM particles. Vlákna a textil 9(4) 149–154, 2002
[9] Murárová A.: Thermal management in a fibre-air system. In: International conference and exhibition a Fibrous materials –XXI century", 23–28. 5. 2005, Saint Petersburg, Russia
[10] Mecheels J.: Korper- Klima-Kleidung. Verlag Schiele und Schon, Berlin 1998
[11] Murárová A., Želinská K.: Evaluation of the thermophysical properties of integrated textile layers. In. Proceeding of the 4th Central European Conference 6.9.–9.9. 2005 TUL Liberec 2005
[12] Suprun N.: Modeling the structural geometry of textile fabrics. Vlákna a textil 11(1) 23–26, 2004
[13] Hes L.: Thermal Properties of Non-wovens. In: Congress Index 87, Geneve 1987
[14] Onder E., Sarier N.: Improving thermal regulatory functions of textiles, 4th AUTEX Conference 2004, Roubaix 2004

Received: September 2005

Termofyziologické vlastnosti integrovaných textilných vrstiev určených do prostredia s extrémne nízkou teplotou

Translation of abstract:

Thermophysiological properties of integrated textile layers designed FOR AN extremely low temperature environment

V príspevku sa pojednáva o termofyziologických vlastnostiach integrovaných textilných vrstiev, ktoré sú vhodné do prostredia s extrémne nízkymi teplotami. Modelová integrovaná textilná vrstva je zložená zo spodnej vrstvy A, vnútornej vrstvy B+i+B a vrchnej vrstvy C, podľa schémy A+(B+i+B)+C. Zvýšená pozornosť sa venuje tepelnému odporu vnútornej tepelneizolačnej vrstvy i a teplovlhkostnému profilu spodnej textilnej vrstve A. Navrhuje sa integrovaná textilná vrstva s vhodnou hrúbkou tepelneizolačnej vrstvy i z netkanej PET textílie, ktorá zabezpečí tepelnú izoláciu organizmu pri minimálnom fyzickom výkone a minimálnej teplote vonkajšej klímy. Teplovlhkostný profil spodnej textilnej vrstvy sa monitoruje pomocou času vysýchania. Zistil sa synergický účinok textilnej vrstvy B na čas vysýchania textilnej vrstvy A.

EFFECT OF A CHANGE IN A FIBRE PATH FROM ONE END OF THE TRANSPORT CHANNEL TO THE ROTOR WALL ON ROTOR-SPUN YARN PROPERTIES

MIRESHGHI S. S., ESKANDARNEJAD S., EHZADAN H.[1], BAMENI MOGHADAM M.[2]

Textile Dept., Science and Research Campus of Tehran Azad University
P.O.Box 14515/4933, Hesarak, Poonak, Tehran IRAN
E-mail: eskandarnejad@yahoo.com

[1]*Textile Dept., Amirkabir University of Technology, Tehran, Iran*

[2]*Statistics Dept., Allameh Tabatabaei University, Tehran, Iran*

The free and uncontrolled flight of fibres from one end of the fibre transport channel to the rotor wall is an important factor affecting the quality of rotor spun yarn. It has been reported that reducing this distance will improve the yarn's quality significantly. In this research, the above distance has been reduced further with three designs in comparison to commercial rotor boxes, and yarn properties such as strength, evenness, imperfections, hairiness, and abrasion were measured. The M1 code was given to the standard model, and M2 to M4 were given to the three proposed designs respectively. The test results showed that tenacity, strain and energy at the peak did not vary significantly, but were at a maximum for the M3 model. The hairiness of the yarn was at a maximum of 4.3 for the M4 model, in comparison to a minimum of 1.2 for the M3 model and 1.7 for the M1 model. Although the machine twist for all the models was the same, the twist of the yarn measured by the untwist-twist method was different. It was at a minimum of 369 t.p.m. for the M3 model, and a maximum of 466 t.p.m. for the M4 model, in comparison to 418 t.p.m. for the M1 model. Due to the different levels of yarn twist, the yarn's abrasion resistance may vary. It was at a maximum of 155 for the M3 model, and a minimum of 90 for the M1 model.

According to the test results, it was concluded that the M4 model would produce a yarn with a maximum level of twist and hairiness. On the other hand, the M3 model would produce a yarn with a minimum level of twist and hairiness and a maximum abrasion resistance of the yarn, which could be useful for the next processing stages.

Introduction

After ring spinning, rotor spinning is the most important yarn manufacturing process, with a continually increasing share of production. A great number of researchers have devoted immense time and efforts to research in this area during the last three decades. As a result, rotor spinning in some industrial countries is over 35 % and approximately 22 % worldwide [1].

Lawrence and Chen have reported that a change in the cross-section of the transport channel of the fibre from a circular to a narrow rectangular one would reduce the degree of freedom of the fibre's configuration within the channel from 3 to 2, which would increase the nearly straight fibres within the channel from 21% to 70 %, in optimized conditions [2&3]. As a result, the cross-section of the fibre transport channel in most rotor spinning machines is almost a narrow rectangular shape instead of a circular one. An increase in the air suction of the rotor box will increase the air flow speed sucked from the opening roller surface into the fibre transport channel, which will improve the fibre transfer from the opening roller into the channel. But this will increase the air flow through the trash ejection slot to the surface of the opening roller, which will bring back the separated trash to the fibre's flow path. Accommodation of an air inlet in the housing of the opening roller after the trash separation point (the knife edge) will allow for the entry of extra air without interfering with the trash separation. This phenomena was introduced by Suessen Company (recently acquired by Rieter), under the

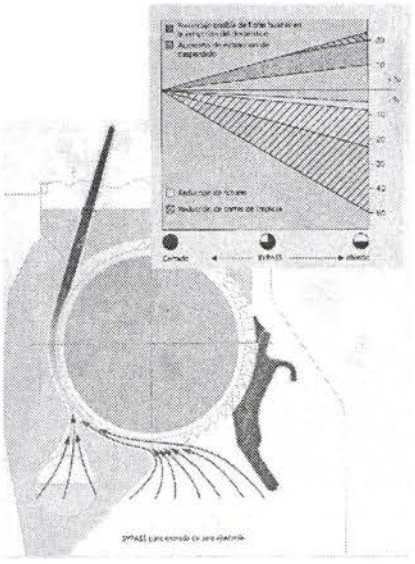

Fig. 1 SC1-M Rotor Spinning Unit of Rieter [4]

name of By-pass in the rotor unit of the SC1-M model [4]. A reduction in the entry of trash to the fibre's flow path will cause the rotor groove to remain cleaner for a

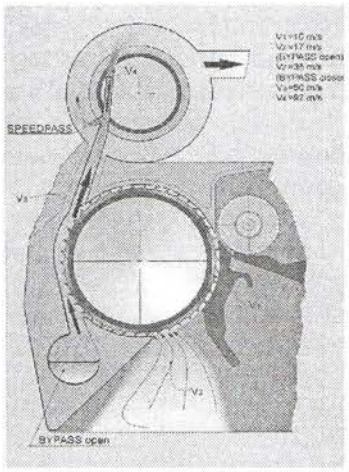

Fig. 2 SC2-M Rotor Spinning Unit of Rieter [5]

longer period of time and improve spinning stability and the yarn's quality. Figure 1 shows a rotor spinning unit with By-pass and its effect on the yarn's breakage rate, trash extracted and the amount of long fibres separated at the trash ejection slot.

Although an increase in air suction from the surface of the opening roller has its advantages, a too high-air flow speed at the end of the transport channel would interfere with the fibre's orientation during its transfer from the transport channel onto the rotor wall or groove. H. Stahlecker has overcome this problem in Speed-pass (SC2-M model) by introducing an extra hole at the end of the fibre transport channel, near the channel exit [5]. As shown in figure 2, the extra air inside the channel will be separated from the fibres before the end of the channel and guided into the rotor box, outside of the rotor. The application of By-pass and Speed-pass in the SC2-M model of Rieter's rotor spinning unit improves yarn strength significantly.

The geometry of the transport channel is another important factor. W. Meier has introduced a fibre transport channel in USP 5,488,822, which has a curved

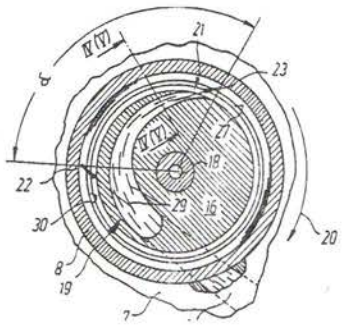

Fig. 3 A Fibre Transport Channel with a Curved Path at the End of the Channel [6]

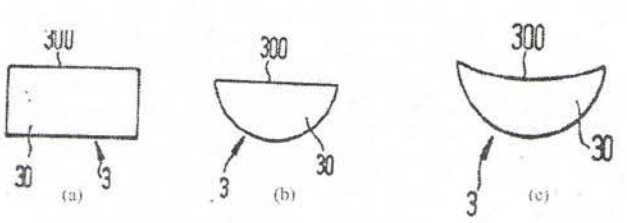

Fig. 4 Cross Section of Channel Exit in W. Billner's Patent [8]

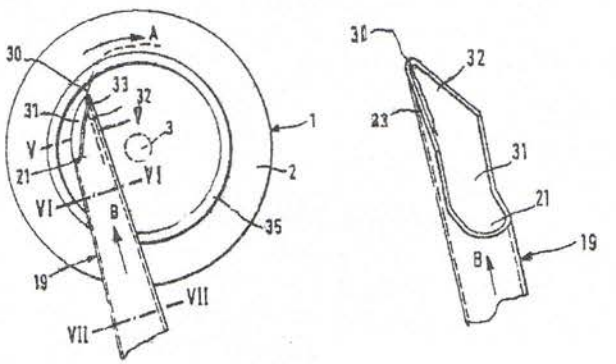

Fig. 5 A Fibre Transport Channel with a Continually Changing Cross-Section [9]

path at the end of the channel [6]. See Figure 3. The advantage of this channel is a reduction in the angle of the fibre's flow axis at the channel exit with respect to the rotor wall, which increases the extent of the fibre in the rotor groove [6].

The cross-sectional area of the fibre transport channel gradually decreases from the channel inlet to the channel outlet and controls the fibre's configuration within the channel. In industrial rotor spinning machines with circular or almost narrow rectangular cross sectional transport channels, the channel axis is not a straight line and is broken before entering the rotor zone. This is for the better guidance of the fibres into the rotor and accessing the rotor wall without an increase in the angle of the fibre's flow axis with respect to the rotor wall, which reduces the extent of the fibre in the rotor groove. This is reported elsewhere by one of the authors of this paper [7]. W. Billner has reported in USP 5,581,991 that fibres would be condensed in one side of the channel after the bending point of the channel axis and would be fed into the rotor wall in a layer form [8]. The fibres are in touch with one side of the channel at the exit. Figure 4 shows the cross sections of the transport channel's exit in this patent. In figures 4a and 4b, fibres are condensed on a flat surface and fed to the rotor in a layer form, while in figure 4c, the surface is a convex one and will better spread the fibres on the rotor wall than in previous cases [8].

F. Stahlecker has introduced a fibre transport channel in USP 4,858,423, in which the channel's cross section changes continuously from a round portion via an approximately oval portion toward a groove shape [9]. Figures 5 and 6 show the channel and its cross sec-

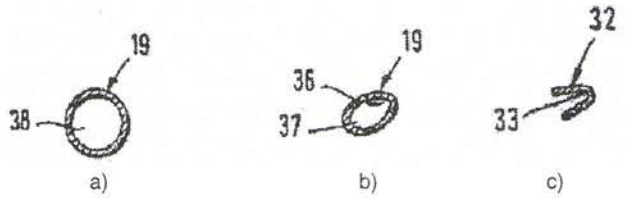

Fig. 6 Cross Section of Stahlecker's Channel in Chronological Order [9]

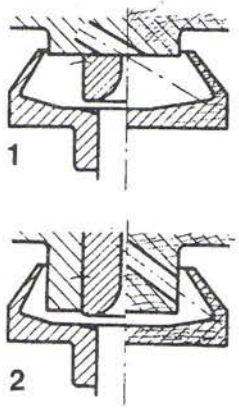

Fig. 7 Rieter's A&U Rotor Spinning Unit Model [10]

tions. Since the fibre transport channel at its end area is formed only of a groove, it is possible without any difficulty to place the channel far in the edge area of the rotor cover, so that its generating line, which is located on the outside in a radial direction, extends approximately tangentially with respect to the outer circumference of the rotor cover. As a result, there would be more room for the yarn withdrawal nozzle and a longer extent of the fibre on the rotor wall during spinning.

The air flow between the end of the transport channel and the rotor wall is turbulent, and there is no control on the fibre's orientation during its free flight within this distance. H. Stalder has reported that reducing the distance of the fibre transport channel and the rotor wall in Rieter's rotor spinning unit of the U model (side feed) will improve the yarn's quality significantly with respect to its predecessor unit, the A model [10]. The yarn mass irregularity and nep count will decrease by 1 to 5 % and 6% respectively. The yarn's tenacity will increase 10 %, and it will be more useful for finer fibres. Figure 7 shows Rieter's A and U rotor spinning unit models. Figure 7 shows Rieter's A&U rotor spinning model [10].

It may be concluded from a review of the literature that the transport channel is an important part of the rotor spinning unit and is suitable for further research. The aim of this research was to further reduce the free flight distance of the fibres in side-feed units in order to improve the yarn quality.

Materials and Methods

The material used was 38 mm, 1.7 dtex viscose fibre. The experimental rig was a Rieter RU04 rotor spinning unit with four individually controlled motors for a driving sliver feed, beater, rotor and winding unit, and a suction pump. The feed sliver and yarn counts were 0.14 Ne and 43 Tex respectively. The feed rate, speed of opening roller, rotor and yarn delivery was 0.619 m/min, 6,000 rpm, 50,000 rpm and 70 m/min respectively.

In order to reduce the free flight of the fibre inside the rotor box, three transport channels were designed and tested. The standard channel of Rieter was identified with the code M_1, and the second channel (M_2), which is made of a conical part joined to a cylindrical extension as a channel exit, was located inside the original channel. When the rotor cover is closed, the M_2 channel can slide further down to reduce its distance from the rotor wall. It is obvious that before opening the rotor cover, the channel must slide upward to prevent

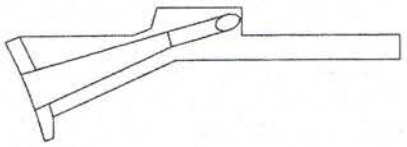

Fig. 8 Schematic Diagram of the Standard Transport Channel (M_1)

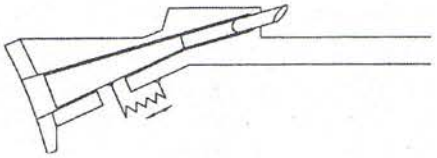

Fig. 9 Schematic Diagram of the Sliding Transport Channel (M_2)

the impact between the channel's exit and the rotor wall. Figures 8 and 9 show a schematic diagram of the M_1 and M_2 channels.

The 3rd channel (M_3) was the same as the original one, but with a telescopic extension at its end. Once

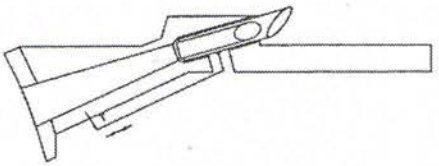

Fig. 10 Schematic Diagram of the Telescopic Transport Channel (M_3)

again, after closing the rotor cover, the telescopic part was able to move towards the rotor wall and reduce the distance. See Fig. 10.

In the last design, the channel remained unchanged, but the part of the rotor cover which enters inside the rotor, was made moveable along the fibre path. After closing the rotor cover, the moveable part moves outward and reduces the fibre path from the channel exit to the rotor wall. See Fig. 11.

The yarns were tested for strength, evenness and imperfections, hairiness, abrasion and twist. The yarn's strength was measured on a SDL yarn strength tester

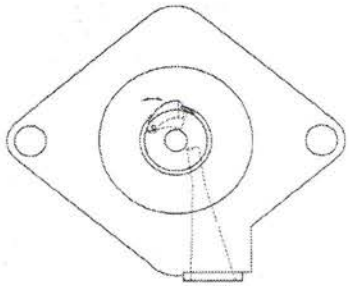

Fig. 11 Schematic Diagram of Final Model (M_4)

with a constant rate of extension (CRE), a clamp speed of 999 mm/min, and a gauge length of 500 mm. Thirty samples were tested in each case. The yarn's evenness and imperfections were tested on a Superba CRM model yarn tester at a speed of 200 m/min, and four samples were tested for each model. The hairiness of the yarns was measured on a SDL hairiness tester for hairs equal to and longer than 3mm.

The yarn speed was 30m/min, and 5 samples were tested in each case. Therefore, 150 m of each yarn was tested. The abrasion resistance of the yarns was tested on an SDL yarn abrasion tester which rubbed the yarn against a bare polished metal rod.

The twist of the yarns was measured on a Shirly twist tester with the untwist-twist technique, and used a gauge length of 50 Cm, an extension allowance of 6 mm and a tension of 15 g, as suggested by the manufacturer. Thirty samples were tested in each case. The test results were analyzed by ANOVA for any difference between the means and by Dunnett for comparison with the original channel [11[.

A Duncan test was also carried out for the comparison of any two models [11].

Discussion of the Results

The results of the tenacity, extension and rupture work of the yarns are given in Figs. 12 and 13. None of these yarn properties changed dramatically, and the analyses of the variance (ANOVA) also did not show any significant difference.

The results of the evenness and imperfections are given in Fig.14. It is quite clear from the results that there is no difference between the mass CV% and the amount of thin places of the yarn, but it is different for the thick places and neps. The amount of thick places was at a maximum in the M_1 model and a minimum in the M_4 model. The amount of neps was zero in the M_1 and M_3 model (as measured) and of a maximum in the M_4 model.

The results of the hairiness, abrasion resistance and yarn twist are given in Figs. 15, 16 and 17. The hairiness of the M_4 model was at a maximum (4.32), and M_3 model was at a minimum (1.20). The hairiness of the original model (M_1) was 1.70.

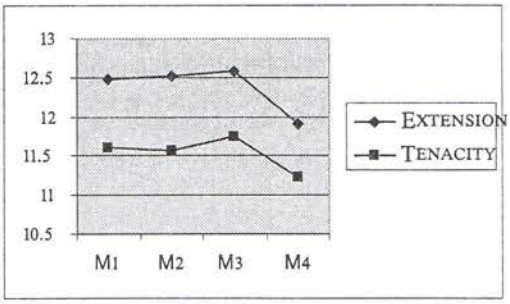

Fig. 12 Tenacity and Extension for Different Models

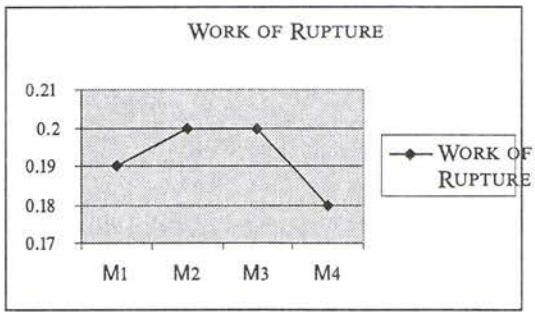

Fig. 13 Work of Rupture for Different Models (N.m)

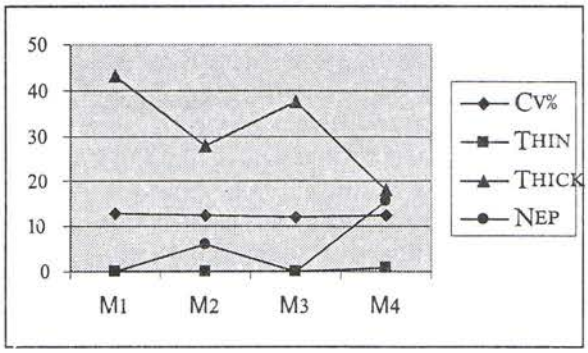

Fig. 14 Yarn Mass CV% and Imperfections for Different Models

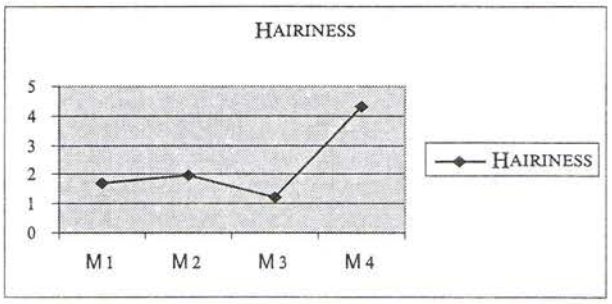

Fig. 15 Yarn Hairiness for Different Models

The yarn's abrasion resistance was at a maximum for the M_3 model (155.5), and at a minimum for the M_1 model (88.6). But due to a high CV% of these results, their confidence coefficient will be lower than normal.

The twist of the yarns varied for different models; it was at a maximum for the M_4 model (469), and a minimum for the M_3 model (369). Twist of the original

model (M_1) was 418 t.p.m.

It should be noted that there was a big difference between the twist of the yarns of the M3 and M4 models, and care should be taken to avoid misjudgments.

The wrapper fibres of the rotor spun yarns affect the result of the twist measurements when using the untwist - twist technique. Since there was a significant difference between the twist of the M_4 and M_3 models, it was decided to examine the surface of the yarns for wrapper fibres. The surface of the yarns was studied under a projection microscope and SEM for the wrapper fibre arrangement. Figs. 18 to 25 show SEM photographs of the surface of the yarns. The wrappers of the M_1 and M_2 models were nearly the same, but the M_3 & M_4 were different. In the M_3 model the wrapper fibres were so tight that the diameter of the yarn at this point was visibly lower than the diameter of the other parts of the yarn. This may restrict the movement of the fibres during twist measurements using the untwist-twist method and may resemble a lower twist and increase the abrasion resistance of the yarn. Also, tight wrapping may reduce the yarn's hairiness, which was the case with the results of the above tests. In the M_4 model, the wrappers were very loose. In some parts they were spread along the yarn, and in other parts, a group of fibres was wrapped loosely around the yarn which produced a loose cork-screw structure. The loose wrappers of the M_4 model may increase the value of the twist measured and increase the hairiness and nep of the yarn, which corresponds to the results obtained.

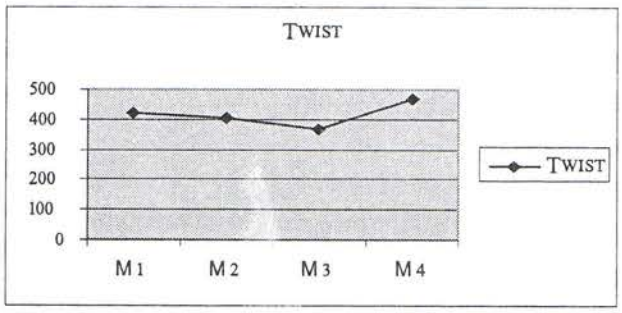

Fig. 17 Yarn Twist for Different Models

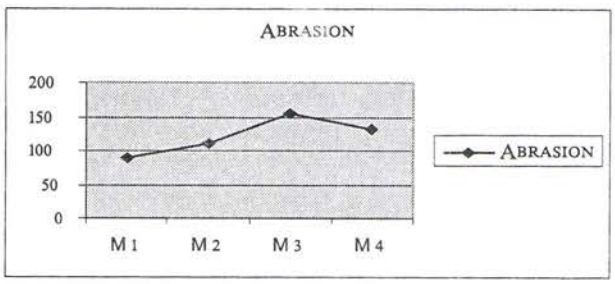

Fig. 16 Yarn Abrasion for Different Models

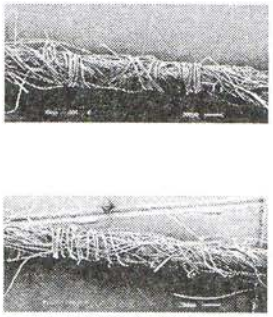

Fig.18&19 Wrapper Fibre of the Standard Channel (Normal)

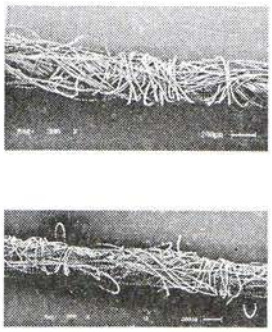

Fig. 20 & 21 Wrapper Fibre of the Sliding Channel (Normal)

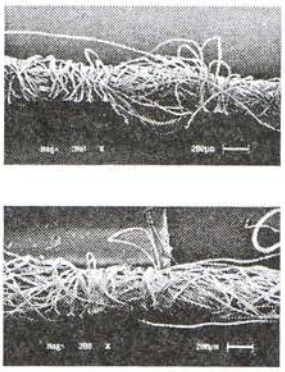

Fig. 22&23 Wrapper Fibre of the Telescopic Channel (Tight)

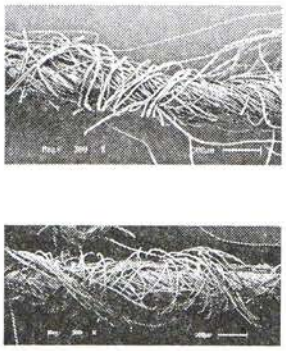

Fig. 24&25 Wrapper Fibre of the Final Model (Loose - Extended & Cork Screw)

Conclusion

In this research three newly developed transport channels of a rotor spinning system were introduced and tested. According to the test results it was concluded that:

1. The M_2 model reduces the number of thick places, was nearly similar to the original model, and did not change the yarn's other properties.
2. The M_4 model produces a yarn with a minimum number of thick places, but with maximum hairiness, twist, number of neps and loose wrapper fibres.
3. The M_3 model produces a yarn with minimum hairiness, twist and maximum abrasion resistance together with tight wrapper fibres.

From the three designs, the M_3 model, which was the telescopic one, was the best and produced a yarn with improved yarn properties.

References

[1] G. Trommer: *Rotor Spinning*, Melliand, 1995

[2] C. A. Lawrence and K. Z. Chen: *A Study of the Fibre Transport Channel Design in Rotor Spinning, Part I: The Fibre Trajectory*, J.T.I., Vol. 79, 1988, No. 3, pp. 367–392

[3] C. A. Lawrence and K. Z. Chen: *A Study of the Fibre Transport Channel Design in Rotor Spinning, Part II: Optimization of the Transport Channel Design*, J.T.I., Vol. 79, 1988, No. 3, pp 393–408

[4] "Commercial Catalogue of Compact Spinning Box SC1-M", published by Spindle Fabric Suessen, pp 4–15.

[5] "Commercial Catalogue of Compact Spinning Box SC2-M, With By-pass and Speed-pass", published by Spindle Fabric Suessen, pp 4–15

[6] W. Meier: *Curved Fibre Guide Channel For an Open-End Spinning Apparatus*, U.S.P. 5,488,822, February 1996

[7] S. Eskandarnejad: *A Study of Fibre Behaviour in the Transfer Zone of an Open-End Spinning System*, Ph.D. Thesis, Textile Department, University of Manchester, UMIST, 1991

[8] W. Billner: *Passing Through the Fibre Collection Groove*, U.S.P. 5,581,991, December 1996

[9] H. Stahlecker: *Fibre Feeding Arrangement for Open-End Rotor Spinning*, U.S.P. 4,858,423, August 1989

[10] H. Stahlecker: *Spinning Fine Yarn Counts on O.E. Machines*, I.T.B., 2/1979, Spinning, pp 155–173

[11] Charles R. Hicks: *Fundamental Concepts in the Design of Experiments*, Third Edition, Holt-Saunders

Received: August 2005

Efekt zmeny na dráhe vlákna z jedného konca transportného kanála k rotorovej stene na vlastnosti rotorovo zvlákňovaných priadzí

Translation of abstrakt:

Effect of a change in a fibre path from one end of the transport channel to the rotor wall on rotor–spun yarn properties

Voľný a nekontrolovaný let vlákien z jedného konca transportného kanála k rotorovej stene je dôležitý faktor ovplyvňujúci kvalitu rotorovo zvlákňovaných priadzí. Bolo zistené, že skrátenie tejto vzdialenosti podstatne zlepší kvalitu priadze. V tomto príspevku bola táto vzdialenosť ďalej znížená tromi spôsobmi v porovnaní s komerčnými rotorovými zariadeniami a boli merané vlastnosti priadzí ako pevnosť, rovnomernosť, chlpatosť a oder. Štandardný model je označený M1, M2 - M4 je označenie troch použitých modelov.

Výsledky testov ukázali, že pevnosť a deformácia sa podstatne nemení, ale maximálna bola pre model M3. Maximálna chlpatosť priadze pre model M4 bola 4,3 ~ v porovnaní s minimom 1,2 pre model M3 a 1,7 pre model M1. Hoci zákrut udelený zariadením bol pre všetky modely rovnaký, zákrut priadzí, meraný metódou zakrúcanie – odkrúcanie, bol rozdielny. Minimálny zákrut – 369/m bol pre model M3, maximálny zákrut 466/m bol pre M4 model v porovnaní s 418/m pre štandard M1. Dôsledkom rôznej úrovne zákrutu priadzí sa môže meniť oderuvzdornosť priadzí. Maximálna oderuvzdornosť 155 bola pre model M3 a minimálna 90 pre štandard M1. Podľa dosiahnutých výsledkov možno usúdiť, že model M4 by mohol dávať priadzu s maximálnou úrovňou zákrutov a chlpatosti. Naopak model M3 by mohol dávať priadzu s minimálnymi zákrutami a chlpatosťou a maximálnou oderuvzdornosťou, čo by mohlo byť užitočné pre ďalšie stupne spracovania.

Efekt zmeny na dráhe vlákna z jedného konca transportného kanála k rotorovej stene na vlastnosti rotorovo zvlákňovaných priadzí.

LIGHTFASTNESS OF REACTIVE DYES

Vassileva V.*, Jeleva J.

*University of Chemical Technology and Metallurgy, Department of Technology of Textile Fibers, 1756 Sofia, 8 Kl. Ohridski st., Bulgaria, *violet@uctm.edu*

The light-fastness of nine reactive dyes was investigated under natural conditions. The decrease in intensity of the color systems of the experimental samples, which resulted from the occurrence of photodestruction processes, was determined using the Kubelka-Munk function. The kinetic study revealed that blue dyestuff systems have the highest degree of lightfastness. They are followed by red dyes, and yellow dyes are in third place with the exception of Bezaktiv Gelb V-GR. When the concentration of the dyes is increased, their degree of fastness improves.

Introduction

Reactive dyes are bright and brilliant and cover the whole color range. Due to the strong covalent bonds between dyestuff molecules and fiber functional groups, their colors are highly resistant to washing and friction. Lightfastness is another important property limiting the lifecycle of dyed textile materials. It is particularly important for products such as summer clothing and sportswear used under conditions of extensive sunshine. In this case it is preferred that fibers and dyestuff possess a comparable fastness, but this is practically hard to achieve.

The combined impact of sunshine and other outdoor factors such as temperature, moisture content, and chemical composition of the atmosphere induce photodestruction of fibers and photofading of dyestuffs. The processes that occur are mostly photo-oxidative and depend strongly not only on the above-mentioned factors, but also on the chemical composition of dyestuffs, their concentration and the type of media in which they are distributed [1-4]. This study is aimed at the effect of chemical structure and the concentration of dyestuff on their lightfastness.

Materials and methods

Nine reactive dyes representing three different reactive groups, which were produced by Bezema Co, as shown in Table 1, were used in the experimental study. They were used for treating a 100% cotton fabric following the technology of the dye-producing company.

The experimental samples were dyed with dyes from the groups HE and S in two concentrations – 1% (low) and 4% (high). Two concentrations were used for studies with the V group dyes – 10 g/l (low) and 50 g/l (high).

The light irradiation occurred under natural conditions by varying the impact time in a range from 30 to 150 hours.

Table 1 Trade names of the dyes used:

No	Name of Dyestuff	Reactive group
1	Bezaktiv Gelb HE-6G	Monochlorotriazine
2	Bezaktiv Rot HE- 7B	
3	Bezaktiv Blau HE-GX 145	
4	Bezaktiv Gelb S-8G	Vinyl-sulphone and Monochlorotriazine
5	Bezaktiv Rot S- 3B	
6	Bezaktiv Blau S- FR 150	
7	Bezaktiv Gelb V – GR	Vinyl-sulphone
8	Bezaktiv Rot V- BN	
9	Bezaktiv Blau V- R Spez	

The variation in color intensity resulting from the photodestruction that occurred was measured by the Data Color system.

A thin layer chromatographic (TLC) analysis was carried out using silica gel plates (Merck Kieselgel 60) in accordance with [5,6]. Unsatisfactory results were obtained when comparing the chromatographic systems investigated with the reference data.

Results and discussion

1. Photofading of dyestuff:

Dyestuffs are complex organic substances, and the destruction of their chromophore system may occur as a result of oxidative or reduction mechanisms. Due to difficulties in the determination of the intermediate and final destruction, product postulates are used by many researchers.

The chromophore systems of the reactive dye comprise the following chemical structures: azo-, azo-metallic complexes, anthraquinone and phtalocyianine.

It is well known that the most popular type of synthetic dyestuffs have an azo structure which is not charac-

terized by a high degree fastness. The production of a dyestuff with improved light-fastness is feasible through the use of selection and substitution. This refers to reactive dyestuffs with fast colors under conditions of exploitation on the basis of covalent bonding with the fibers. Azo-dyes mainly cover the yellow-red color range. One of the options for improving lightfastness is the formation of metal complexes. Anthraquinone and phtalocyanine structures have significantly higher lightfastness indexes and are preferred for the blue-green color range.

As already noted, the factors determining lightfastness are complex and numerous. Chemical structure and concentration of the dyestuff are the primary factors affecting fastness due to aggregation, self-extinction of the concentration, the filtration effect, etc.

An increase in the irradiation time results in a higher degree of photodestruction followed by a decreased color intensity as established by (K/S) values. The color intensity of dyed textiles is determined by the Kubelka-Munk function (K/S), which is proportional to the concentration of dye in the fabric. As seen in Figures 1b and 2b, the (K/S) values decrease when the irradiation time grows. Figures 1a and 2a present the remission curves of the experimental samples on whose basis the selection of λ_{min} for the (K/S) determination was done.

Similar curves were obtained for the other dyestuffs studied.

Figure 3a reveals that the kinetic curves have different slopes, which indicate differences in the decomposition rate of the various chromophoric systems for the yellow, red and blue dyes. The mechanism of bonding the reactive dyes with fiber-forming polymer functional groups suggests that they are present in a monomolecular state in the matrix. According to Giles [7–9], the kinetic curves of the photofading are of a first order when dyes are present in a monomolecular state or as small size aggregates. One characteristic of the first order reactions is the linearization of kinetic curves in a semilogarithmic coordinate system (Figures 3b, 4b, 5b) The line slopes correspond to the rate constants presented in Table 2. The blue dyestuff has the highest degree of fastness, followed by the red and the yellow (Blue >Red>Yellow). This refers to both experimental concentrations.

The effect of the concentration factor on the lightfastness established by other authors but still unexplained is also observed. With a higher concentration, better light fastness values are established for all dyestuffs. The reactive dyes are covalently bonded to cellulose hydroxyl groups that prevent the formation of casual aggregates. It can be suggested that the concentration effect consists in "concentration self-extinction" [10] as the concentration gradient ensures the distance enabling the energy transfer from the dye. The occurrence of an energy "discharge" of excited molecules decreases the probability of their participation in further photodestruction reactions.

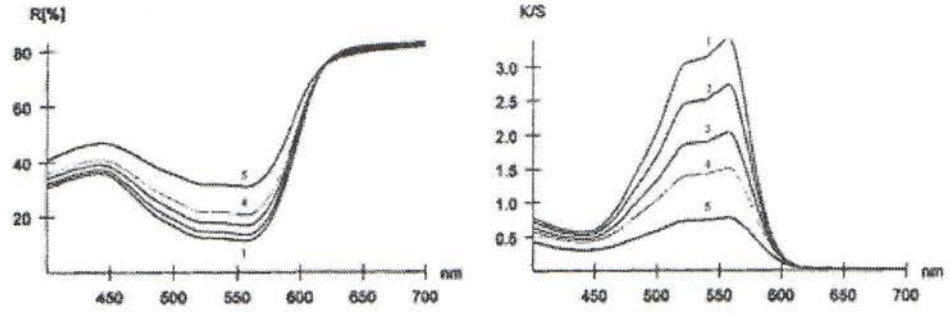

Fig. 1 Remision curves (a) and K/S values (b) of Bezaktive Rot HE-7B dye at various irradiation times: 1 – 30 h, 2 – 60 h, 3 – 90 h, 4 – 120 h,

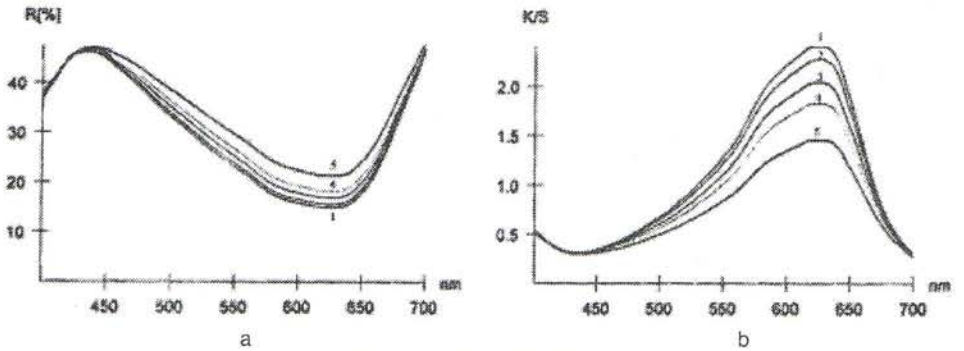

Fig. 2 Remision curves (a) and K/S values (b) of Bezaktive Blau S-3FR dye at various irradiation times: 1 – 30 h, 2 – 60 h, 3 – 90 h, 4 – 120 h,

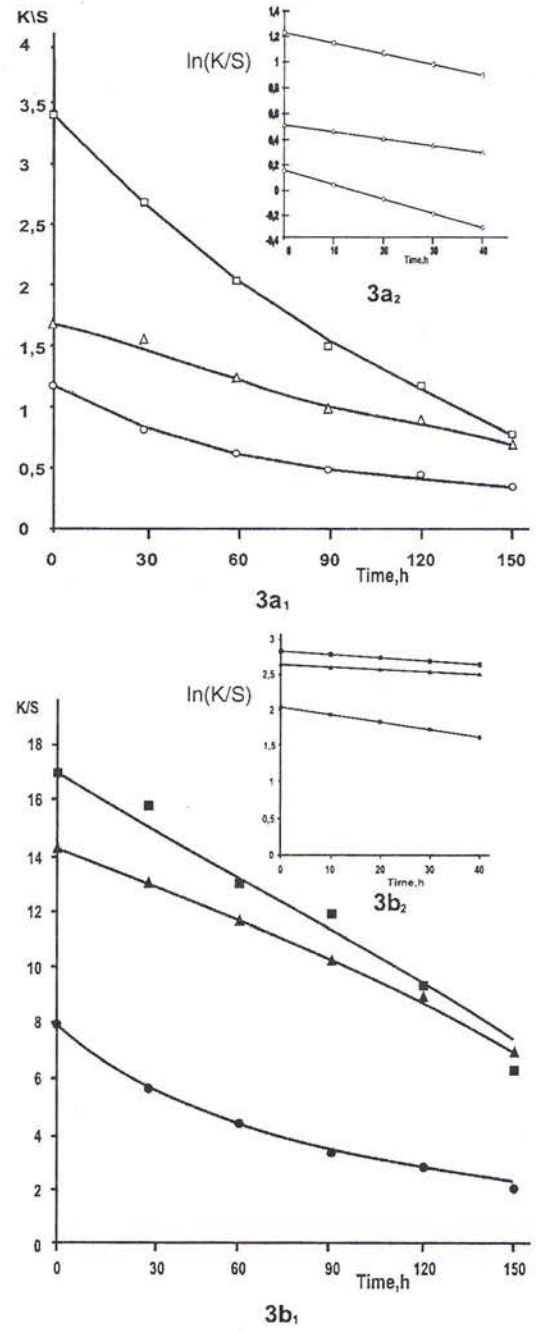

Fig. 3 Kinetics of Bezaktive HE dyes photofading: a – 1% dye: ○ – yellow, △ – blue, □ – red; b – 4% dye: ● – yellow, ▲ – blue, ■ – red;

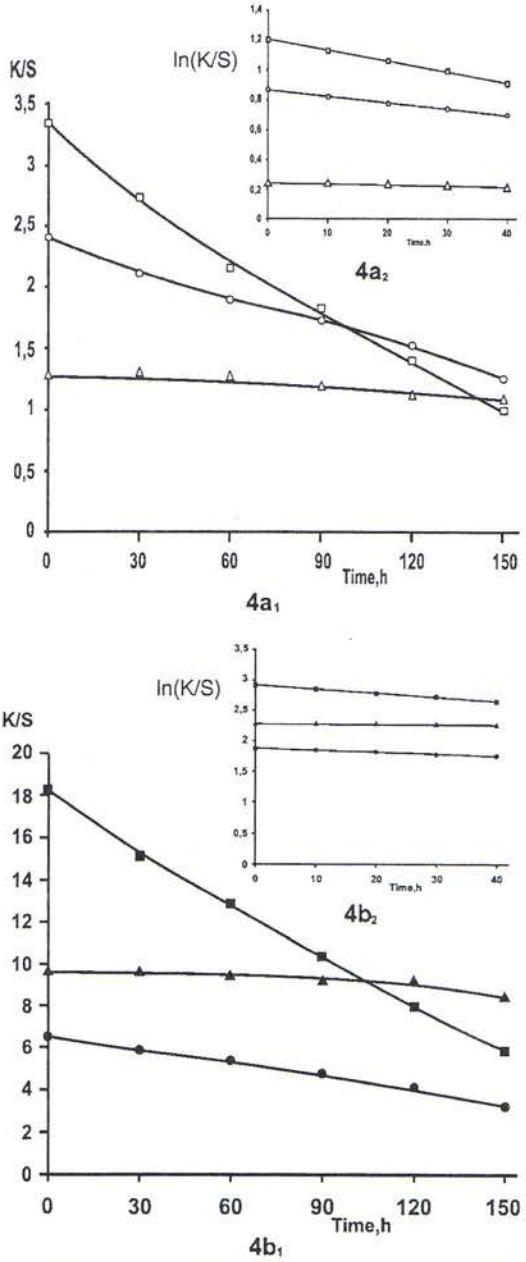

Fig. 4 Kinetics of Bezaktive V dyes photofading: a – 10 g dye/dm^3: ○ – yellow, △ – blue, □ – red; b – 10 g dye/dm^3: ● – yellow, ▲ – blue, ■ – red;

The analysis conducted for the photofading of the group mentioned above is also valid for the Bezaktiv V dyes. As evidenced by Figure 4, the blue dyestuff has the highest degree of lightfastness. In this dyestuff group, the yellow has a better degree of fastness than the red, which occupies last place.

Among all the dyestuffs studied Bezactiv blau V-R has the highest degree of fastness and a correspondingly lower rate of constancy. This result is not surprising, as it has been established that it has an anthraquinone structure – see Figure 6. The dyes may be ordered in the following range of descending lightfastness: Blue >Yellow>Red. . The concentration effect was established for all three dyes as the higher concentration ensures a better degree of lightfastness.

Bezaktiv S is a group of bifunctional dyestuffs incorporating mono-chlorotriazine and vinyl-sulphone reactive groups in a single molecule – see Figure 5. The decrease in lightfastness observed was in the following order:

Blue >Red>Yellow

When the concentration of these dyestuffs is increased, it results in a similar increase in light-fastness of the color systems observed.

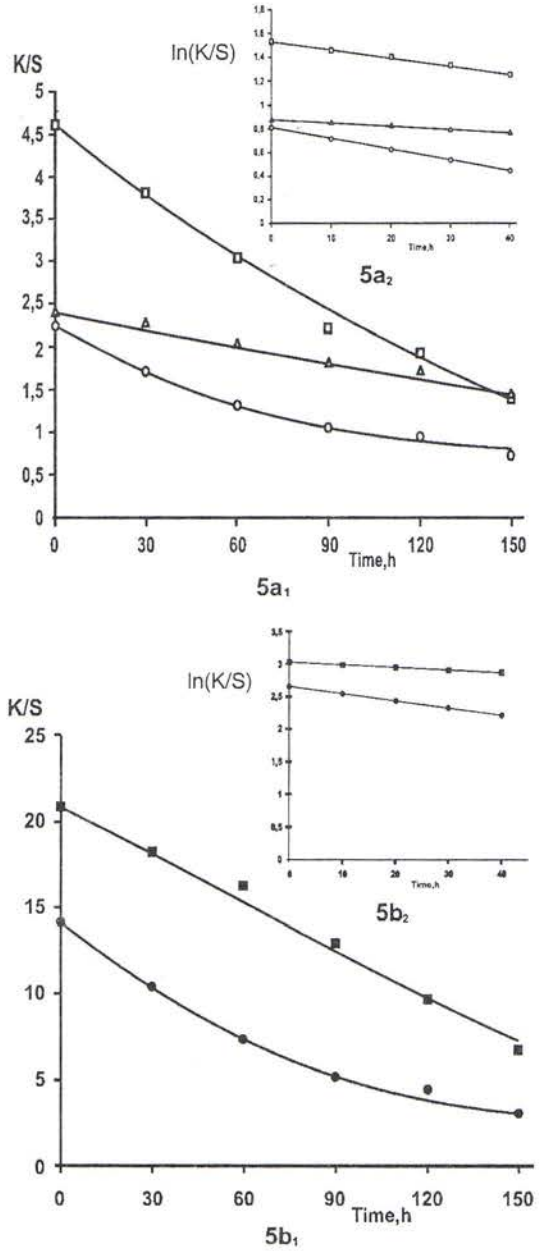

Fig. 5 Kinetics of Bezaktive S dyes photofading: a – 1% dye: O – yellow, △ – blue, □ – red; b – 4% dye: ● – yellow, ▲ – blue, ■ – red;

2. Thin layer chromatographic (TCL) analysis:

TLC is a quick and highly sensitive analytical method for the separation and identification of component mixtures, even in cases when they comprise homologous compounds. The separation is based on the difference in solubility of the corresponding molecules. For this reason dyestuffs with an identical color (the same chromophore system) but with different reactive groups have different chromatographic behaviors.

The separation of a dyestuff takes place in the original n-butyl alcohol chromotagraphic: dimethylformamide: water = 3 : 0,5 : 1.4. As seen in Figure 6, the system is very good as dyestuff systems separate into a maximum number of spots which are well shaped and have different R_f -values. No diffusional spots, initial precipitation and entailing is observed in the TLC system.

Although Bezaktiv Rot HE-7B and Bezaktiv Rot S-3B are identical colors, they have a different number of spots with different R_f- values.

Bezaktiv Blau V-R and CI Reactive Blau 19 have similar chromatographic behavior – a similar spot number, and the same color and spectra, indicating that they have the same structure.

The absorption curve shapes and λ_{max} values of C.I. Reactive Blue 19 (used as a control) and Bezaktiv Blau V-R suggest the existence of identical structures.

The results obtained from TLC analysis lead to the assumption that an identity study is relevant to counter products, while the identity of a chromophore system may be proved by spectrophotometry.

Table 2 Photo-destruction rate constants of the reactive dyes studied.

No	Dyes	Low concentration of dye $k_{1\%} \times 10^3$	High Concentration of dye $k_{4\%} \times 10^3$
1	Yellow HE	11.1	10.5
2	Red HE	8.3	4.2
3	Blue HE	5.4	3.7
4	Yellow S	9.0	11.25
5	Red S	6.7	4.25
6	Blue S	2.7	-
7	Yellow V	4.25	3.25
8	Red V	7.1	6.75
9	Blue V	0.75	0.5

$k_{1\%}$ and $k_{4\%}$ rate constants for the corresponding dyestuff concentration.

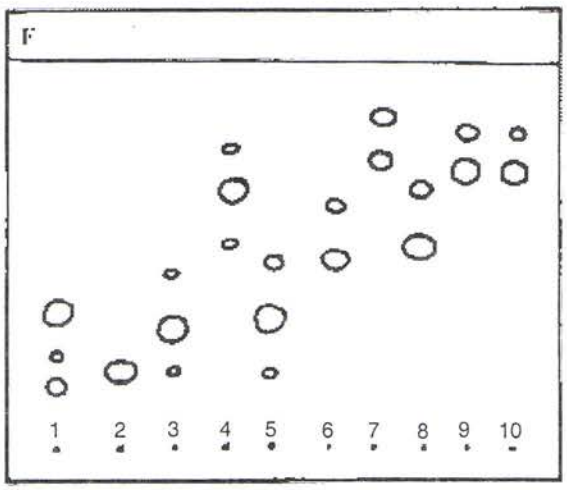

Fig. 6 Thin layer chromatograms of ryes. The numbers correspond to Table 1. No. 10 is CI Reactive Blue 19

Conclusions

The light-fastness of nine reactive dyes representing various reactive groups was investigated. A kinetic study of the photofading of dyes was carried out, and the rate constants were determined. It was established that blue dyestuffs have the highest degree of lightfastness followed by red and yellow dyes. The increased concentration of dyes results in increased lightfastness.

References

[1] Krichevskiy, G. E.: Fotokhimicheskie prevrascheniya krasitelej i svetostabilizatsiya okrashennih materialov, Khimia, Moskva, 1986
[2] Egerton G. S.; Morgan, A. G.: J. Soc. Dyers and Colorists, 86, (1970) pp.79–83
[3] Egerton G. S.; Morgan, A. G., J. Soc. Dyers and Colorists, 86 (1970) pp. 242–249
[4] Egerton G. S., Morgan, A. G.: J. Soc. Dyers and Colorists, 87, (1971) pp.268-277
[5] Ilinov, P.: Tunkosloyna hromatografiya, Sofia, Nauka i Izkustvo., (1988)
[6] Kirchner, J. G.: Tenkosloynaya hromatografiya, Mir, Moscow. (1981)
[7] Giles, C.; McKay, R.: Text. Res. J., 33, (1963) pp. 528–530
[8] C. Giles, J. de Bernat, Textile Res. J., 46, (1976) pp. 673–675
[9] C. Giles, R. Hastman, Textile Res. J., 48, (1978) pp. 490–492.
[10] Krichevskiy G.E., B.Vachobov,Tex. Res. J., 45, (1975) pp. 608–619

Received: December 2005

Svetlostabilita reaktívnych farbív

Translation of abstract:
Lightfastness of Reactive Dyes

Svetlostabilita deviatich reaktívnych farbív bola sledovaná v prirodzených podmienkach. Pokles intenzity farebných systémov experimentálnych vzoriek, vyplývajúcich z výskytu fotodeštrukčného procesu bol určený podľa Kubelka-Munk funkcie. Kinetické štúdium ukázalo, že modré farebné systémy majú vyššiu svetlostabilitu stálosť. Nasledujú červené farbivá a na treťom mieste sú žlté farbivá s výnimkou farbiva Bezaktiv gelb V – 6R. So zvyšujúcou sa koncentráciou farbiva sa zvyšuje stálosť systému.

WETTING OF ANISOTROPIC SURFACES

Wiener J., Dembický J.

Textile Faculty, Technical University of Liberec, Hálkova 6, 461 17 Liberec, Czech Republic
e-mail: jozef.dembicky@vslib.cz, jakub.wiener@vslib.cz

An important parameter in the wetting of textiles is the relative contact angle, which is any angle whose value depends on other parameters of a tested surface than on its chemical composition only. The basis reason for this relativity is the geometry of the surface and its non-homogeneity.

THEORETICAL

The result of a contact angle between liquid, air and a solid state surface with the structure of a solid state surface is given by the contact of the liquid with a jagged surface. Several surfaces (usually the less jagged ones) behave according to the Wenzel model (1), while more jagged surfaces with more porosity behave like the Cassie-Baxter model (2).

The groundwork of the Wenzel model of a rough surface wetting is the concept of a surface that is wetted with liquid, and the contact angle is given by the local angle incline in contact with the liquid. Wenzel presented a model describing the apparent contact angle on a rough surface, as follows:

$$\cos\alpha = d\cos\beta \qquad d = S_2 / S_1 \qquad (1)$$

where d is a factor of roughness defined as a microscopic ratio (real) S_2 and a macroscopic (geometric) S_1 surface area, α a is a real contact angle on flat material according to Young's equation. β is an apparent (macroscopic) contact angle. The surface roughness factor on real surfaces is common over 1; then the fundamental properties of the surface are demonstrated. With the increase in roughness a hydrophobic surface becomes significantly more hydrophobic, and a hydrophilic surface becomes significantly more hydrophilic.

Cassie and Baxter based their model on a concept of a substrate that is not wetted enough, but an air layer can occur between the liquid and the parts of the solid substrate. The contact angle takes place at the interaction with the air and equals 180°.

$$\cos\alpha = f_1\cos\beta + f_2 \qquad (2)$$

The ratio of a liquid contact with a solid substrate is marked f_1. The ratio of a contact with the air is marked as f_2. The Cassie-Baxter model is suitable for all surfaces, but its main advantage is the possibility of theoretically analyzing hydrophobic surface with high surfaces roughness. Thanks to this equation it is possible to clarify the extreme contact angle on jagged surfaces – for example, the surface of a lotus (figure 2).

The higher profile character of a surface leads to a significant demonstration of a given property. If a flat surface is wettable, it will be more wettable after roughening. If a flat surface is hydrophobic, it will be more hydrophobic after roughening. This corresponds with the following picture, where the dependence of the contact angle (α_D) on the surface roughness (d) for different contact angles defined on smooth materials (α_H) is shown. The calculation was done according to Wenzel's equation.

The flat lines connect points with the same actual contact angle. The roughness is shown on the horizontal axis (d, ratio of the actual and apparent surface area), the apparent contact angle is defined on the vertical axis; the data were calculated with the help of an equation (2).

Concerning porous, non-homogenous structures, e.g., textiles, the situation is more complicated than with

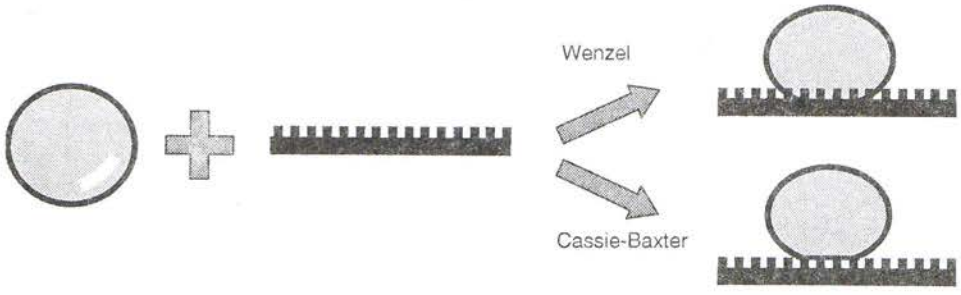

Picture 1. Behavior of a drop of liquid on a jagged surface – the schematically defined difference between the Wenzel and the Cassie-Baxter wetting models.

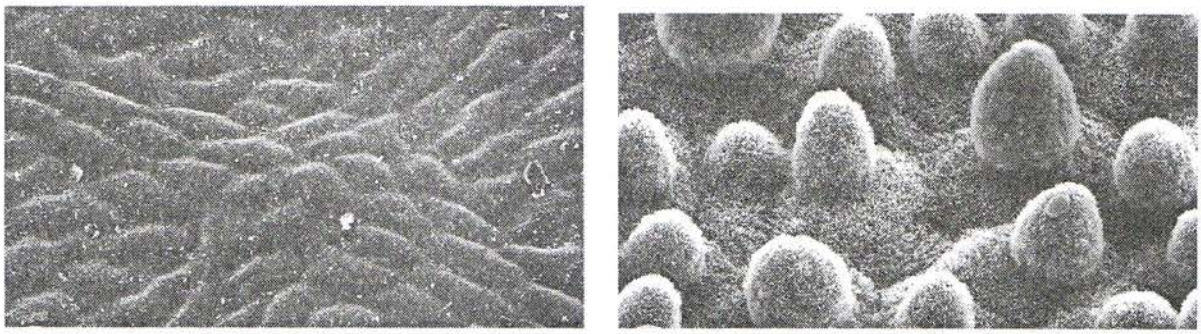

A B

Fig. 2 Impact of surface roughness on the contact angle – a surface of herbs/water; the length of the scale in the picture is 20μm A – beech leaf (Fagus sylvatica, contact angle 72°), B – lotus (Nelumbo lucifera, contact angle 161°)

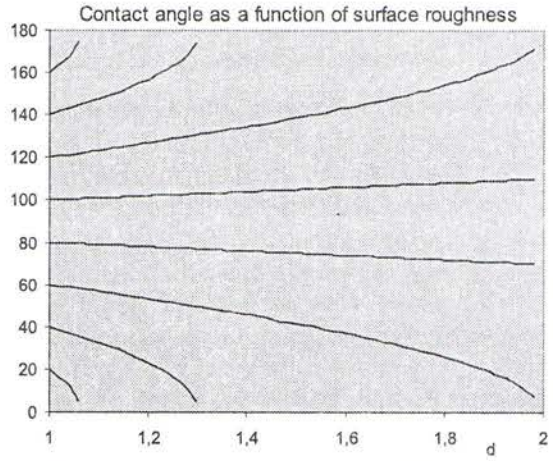

Fig. 3 The change in the contact angle's appearance depending on the surface roughness

homogenous substrates. On ordinary flat materials (for example, glass, a plastic mass, etc.) the contact angle is given through the balance of the surface tensions.

The contact angle on an ideal flat surface is marked as actual. If the surface of the tested material is rough, then the contact angle is established as apparent – it is not consistent with the chemical composition, and it depends on the ratio of roughness of the surface.

The contact angle observed in macroscopic experiments can be significantly different from the value achieved by a calculation of the physical-chemical considerations. The groundwork of the "contention" between a macroscopic (apparent) and an actual contact angle is the geometry of the wetted surface. In the case of homogenous states (for example, a polypropylene sheet), the roughness describes the surface properties.

Concerning porous non-homogenous structures (for example, textiles), the situation is more complicated than with homogenous substrates (see above). Upon the contact of a liquid with a textile material, it is possible to follow the contact angle which is always to be considered as apparent.

In a comparison of the surface structures of herbs, which show extreme hydrophobity with textiles, surprising connections can be found.

Herbs with a high degree of hydrophobity have a jagged surface, where more levels of profel can be identified– the surface is jagged in every magnification. Here are almost macroscopic forms not only, in the decimals of micrometers, but also microstructures in tenths of micrometers. If the herb needs to drain water away, it creates an anisotropic structure on its surface. In this way the herbs achieve boundary contact angles with water of about 160°.

If we look at these textiles from a further distance, we can see the mutual characteristics of the textiles and extremely hydrophobic herbs. Several levels of articulation can also be found in such textiles as yarn, fibers, and fiber roughness in dimensions of units to hundreds of micrometers (figure 5).

On this ground the hydrophobic finishing of textiles is based, where contact angles of 140° can be achieved. Despite the higher porosity of textiles, the contact angles frequently achieved on textiles are not as high

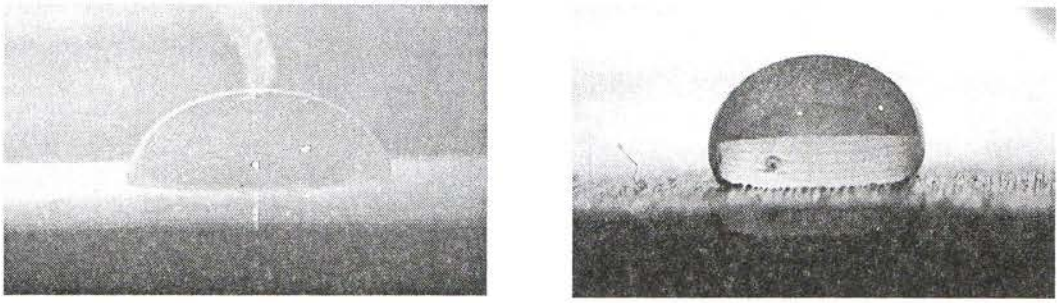

Fig. 4 Form of a sessile drop on a surface of the same composition, but of a different structure: left – the surface is flat (contact angle 90°), right – the surface is jagged (a surface created with 20 μm – diameter parallel fibers – the apparent contact angle is 130°)

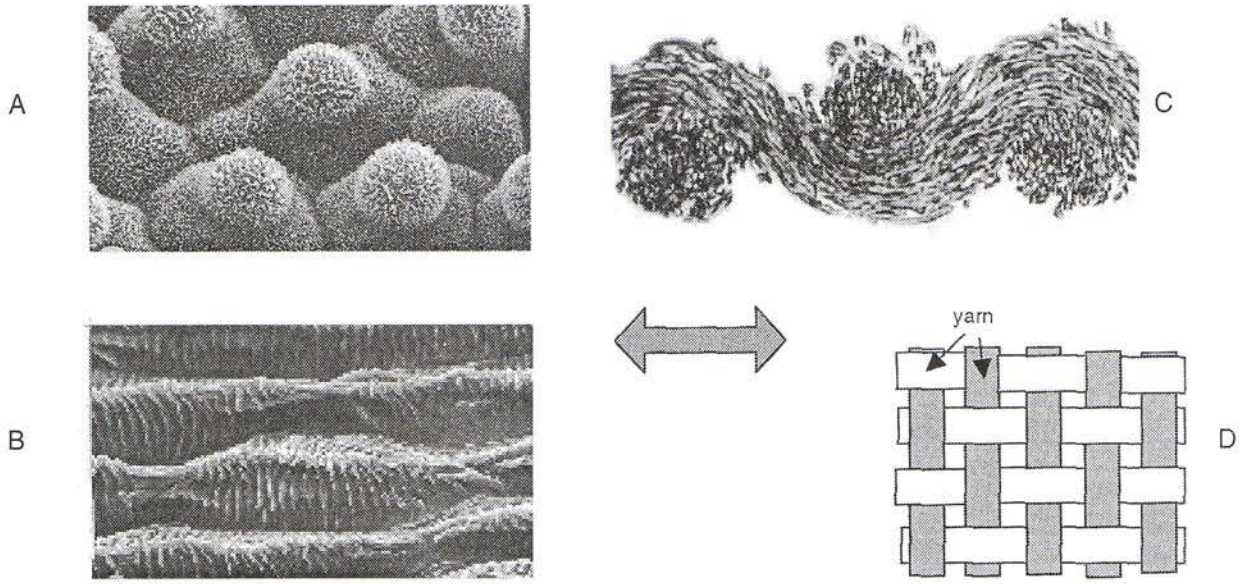

Fig. 5 Comparison of the structure of naturally high hydrophobic surfaces with the structure of a fabric. A – surface of the herb Colocasia esculenta, a picture from an electron microscope, the scale has a length of 20 μm, the contact angle is 160° (water), B – surface of the herb Mutisia decurrens, a picture from an electron microscope, the scale has a length of 20 μm, the contact angle is 160° (water), C – cut through a common fabric made from cotton fibers, D – chart of the structure of a fabric created from yarns

as on certain herbs. The main reason is the difference in the dimension of the surface forms (they are on textile greater than on herbs) and therewith a related surface irregularity.

The impact of roughness on a contact angle can be described through Wenzel's equation, which is valid

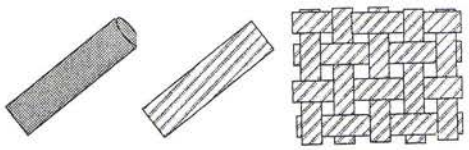

	Fiber	yarn	fabric
hydrophilic	60°	20°	0°
hydrophobic	90°	120°	140°

Fig. 6 Chart of changes of a textile structure and appropriate contact angles with water for different forms of fiber structures – for fiber, yarn and fabric

for the unoriented roughness of a surface. The surface of textiles is anisotropic from the point of view of the contact angles. The simplest surface with similar properties can be a surface with parallel channels on the surface (figure 7).

For anisotropic surfaces (for example figure 7), roughness is to be defined in two directions.

In the direction of the tension activity between a liquid and a solid state (direction of arrow) the surface on the left in figure 7 is not rough – it is perfectly flat. That is why the contact angle in this direction is equal to the contact angle on a flat surface. Young's equation is valid for the contact angle.

In the figure on the right the surface in the direction of the tension activity between a liquid and a solid state (direction of arrow) is jagged; therefore, the Wenzel's equation is valid for the contact angle. According to Wenzel's equation, the contact angle in this direction is more extreme than on flat surfaces. If the flat surface is, for example, hydrophobic, then it is extremely hydrophobic in this direction.

On this ground it is necessary to generalize a coefficient of roughness according to the following scheme – equation (3). Roughness cannot only be defined as the ratio of an actual and macroscopic area, but it can also be defined as a ratio of the interface lengths – the actual and the macroscopic.

$$d = S_2 / S_1 \rightarrow d = L_2 / L_1 \qquad (3)$$

d – coefficient of the surface roughness, ratio of the actual surface area and the apparent (macroscopic) surface area S_1 – area of the actual interface, S_2 – area of the macroscopic interface, L_1 – actual length of the interface in the direction of the surface tension activity, L_2 – macroscopic length of the interface in the direction of the surface tension activity

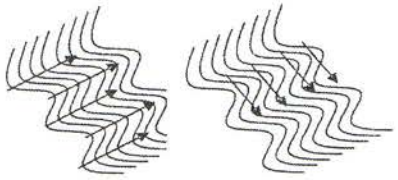

Fig. 7 Schematic illustration of the impact of channels on wetting. On the left wetting in the direction of the channels is demonstrated; on the right it is across the channels.

A surface created with parallel fibers is closer to textiles than a surface created with channels. The monitoring of the distance and the orientation of fibers on the surface impact was conducted on a surface created with parallel fibers.

This structure is easier to define and analyze mathematically than ordinary fabrics, but the same rules must always be applied – the structure is precisely organized and created by the textile fibers. The resulting model's structure has a noticeable anisotropy, which is clear from picture 8.

EXPERIMENTAL

The surface in this experiment was created by twisting a layer of fibers parallel to a dense contact with a solid base; therefore, the fibers did not cross and were mutually parallel.

Special equipment which allowed for the changing of the ratio of inclination and the number of fiber layers was used. For the sake of convenience, monofil fibers higher in diameter or multifilaments in the case of very fine fibers were used. The diameter of the fibers used varied from 10 to 500 μm. The surface of the structure created was hydrophobized by a thin hydrophobic layer on the basis of the perfluorcarbon.

On the surface tested a 20 μl (20 mm^3) drop was applied with a micropipette. The drop was scanned in two directions – see the following scheme. Consequently, a drop was added to the already sessile drop, and this new drop was scanned in two directions again. In this way the volume of the drop was increased till it was 100 μl.

The scanning directions are schematically shown (marked as A and B) with appropriate profiles of the drops in the given directions.

When fibers are dense in contact, the apparent contact angle in the direction of scanning A is about 150°; in this case the actual contact angle is 90°, and the sessile drop is at least of the same high order in dimension as the fiber diameter. With the increasing distance of the neighboring fibers, the maximal value of the apparent contact angle increases – theoretically to 180°. If the fibers are greatly distanced, the liquid will not remain on them – it will run down the fibers.

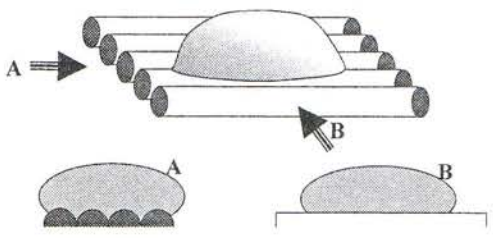

Fig. 8 Schematic picture of an anisotropic surface created by parallel fibers in dense contact

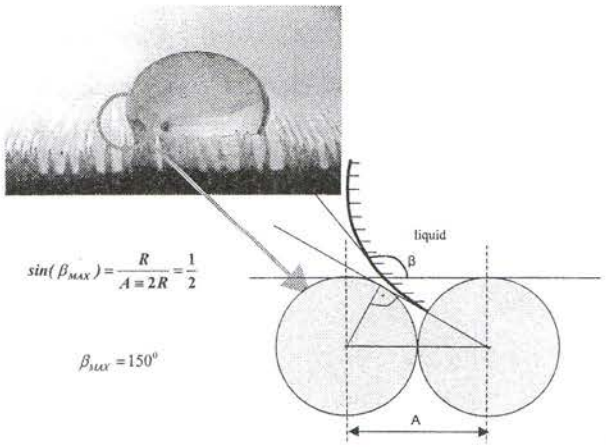

Fig. 9 An anisotropic surface created by parallel fibres with a diameter of about 500 μm – scanning in the direction A, a picture and the groundwork of the physical analysis of the apparent contakt angle

In this case when the fibers are dense in contact the apparent contact angle in the direction B equals 90°; in this case the actual contact angle is 90°. With the increasing distance of the neighboring fibers, the value of the apparent contact angle increases too – theoretically up to 180°. If the fibers are very far apart, then the liquid will not remain on them – it will run down the fibers.

If a system of fibers in dense contact was created, and a drop was placed on this surface at the actual contact angle of 90°, then an apparent contact angle of up to 150° should be observed according to the ideas discussed in the A direction and 90° in the direction of B. This surface was created and an experimental contact angle of up to 140° in the A direction was found; in the B direction, the angle was approximately 110°. These values were measured on fibers of 10 to 500 μm in diameter. The differences between the experiment and the theory are probably caused by breaching the dense contact of the neighboring fibers – the fibers were very difficult to handle - see picture 10 500 μm diameter.

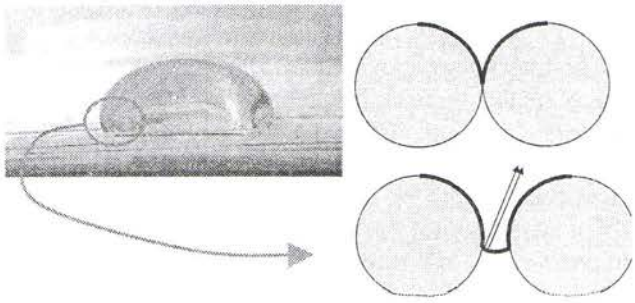

Fig 10 An anisotropic surface created by parallel fibers about 500 μm in diameter – a picture in the direction B, a photo (500 μm diameter fiber) and the groundwork for the apparent contact angle's physical analysis.

CONCLUSION

The contact angles between a liquid and a textile are only apparent – their value is not only given by Young's equation (the equilibrium of the surface tensions), but also by the textile's structure. Great attention was paid to the surface articulation of a fiber structure and its impact on the textile-liquid-air contact angle. A description of a actual textile surface's geometry is not available due to the extremely complicated textile structure and its irregularity. The problem of an actual textile was solved on a simplified, but physically very similar, structural model created by fibers oriented on a parallel – see figure 10. This surface is close to an actual textile in many aspects – the porosity of an actual textile is conserved; the fibers are part of an organized structure, and the structure created is significantly anisotropic. This defined surface can be produced and tested relatively easily. It was shown that in an experimental method, the contact angles are dependent on the orientation in accordance with the proposed theory, and their value is in accordance with the theoretical model designed.

A theoretically more interesting conclusion to these experiments and analyses are findings that in the case of more distant fibers, more extreme contact angles can be achieved. The main determination consists in the fact that through a mechanical change in the distance of fibers on a surface, the hydrophobity of a textile can be changed within relatively wide limits.

REFERENCES

[1] Cassie A. B. D., and Baxter, S. Wettability of porous surfaces, *Trans. Faraday Soc.* 1944, *3*, 16.
[2] Wenzel, R.N.: Ind. Eng. Chem., 1936, 2, 988

Recieved.

SMÁČENÍ VLÁKENNÝCH POVRCHŮ

Translation of Article:
Wetting of anisotropic surfaces

Při sledování smáčivosti textilních materiálů je třeba se zmínit o zdánlivém kontaktním úhlu. Zdánlivým je každý kontaktní úhel, jehož velikost souvisí s jinými parametry testovaného povrchu než jen s jeho chemickým složením. Základním důvodem zdánlivosti je komplikovaná geometrie povrchu a nehomogenita povrchu.

TEORETICKÁ ČAST

Při kontaktu kapaliny s členitým povrchem je výsledný kontaktní úhel mezi kapalinou, vzduchem a pevným povrchem dán strukturou povrchu pevné látky. Některé povrchy (obecně s menší členitostí povrchu) se chovají podle Wenzelova modelu (1), členitější povrchy s větší porozitou podle Cassie-Barterova modelu (2).

Základem Wenzelova modelu smáčivosti drsného povrchu je představa, že povrch je smočen kapalinou a kontaktní úhel je dán lokálním nakloněním povrchu v kontaktu s kapalinou. Wenzel navrhl model popisující zdánlivý kontaktní úhel na drsném povrchu jako:

$$\cos\alpha = d\cos\beta \qquad d = S_2 / S_1 \qquad (1)$$

kde d je faktor drsnosti definovaný jako poměr mikroskopické (skutečné) S_2 a makroskopické (geometrické) S_1 plochy povrchu. α je reálný (skutečný) kontaktní úhel na hladkém materiálu ustavený v souladu s Yungovou rovnicí, β je zdánlivý (makroskopický) kontaktní úhel. Faktor drsnosti povrchu je u reálných povrchů obvykle větší než jedna, pak dochází k zvýraznění základní vlastnosti povrchu. Vlivem nárůstu drsnosti se z hydrofobního povrchu stává povrch výrazně hydrofobnější a z hydrofilního výrazně hydrofilnější.

Cassie a Baxter založili svůj model na představě substrátu, který není obecně kapalinou zcela smočen, ale mezi kapalinou a částmi pevného substrátu se může nacházet vzduchová vrstva. Kontaktní úhel je v místech styku se vzduchem roven 180°.

$$\cos\alpha = f_1\cos\beta + f_2 \qquad (2)$$

Podíl kontaktu kapaliny s pevným substrátem je označen jako f_1. Podíl kontaktu kapaliny se vzduchem je označen jako f_2. Cassie-Baxterův model je vhodný k popisu všech povrchů, ale jeho hlavní výhodou je možnost teoretické analýzy hydrofobních povrchů s vysokou drsností povrchu. Pomocí tohoto vztahu lze vysvětlit extrémní kontaktní úhly na členitých površích – např. povrch lotosu.

Vyšší členitost povrchu vede k výraznějšímu projevu dané vlastnosti: Pokud je hladký povrch smáčivý, bude

po zdrsnění ještě smáčivější. Pokud je hladký povrch nesmáčivý, bude po zdrsnění ještě nesmáčivější. To je v souladu s následujícím obrázkem, kde je vynesena závislost zdánlivého kontaktního úhlu (α_D) na drsnosti povrchu (d) pro různé kontaktní úhly stanovené na hladkých materiálech (α_H). Výpočet byl proveden podle Wenzelovovy rovnice.

U porézních nehomogenních struktur, jejichž příkladem jsou textilie, je situace komplikovanější než u homogenních substrátů. Na běžných plochých materiálech (např. sklo, plastická hmota apod.) je kontaktní úhel dán rovnováhou mezi-povrchových napětí.

Kontaktní úhel na ideálně hladkém povrchu označíme jako reálný. Pokud je povrch testovaného materiálu drsný, pak je stanovený kontaktní úhel zdánlivý - není v souladu s chemickým složením povrchu a je závislý na míře drsnosti povrchu.

Kontaktní úhel zjištěný z makroskopických experimentů se může výrazně lišit od hodnoty stanovené výpočtem z fyzikálně chemických úvah. Základem „rozporu" mezi makroskopickým (zdánlivým) a reálným kontaktním úhlem je geometrie smáčeného povrchu. V případě homogenních látek (např. deska z polypropylénu) popisuje vlastnosti povrchu jeho drsnost.

U porézních nehomogenních struktur, jejichž příkladem jsou textilie, je situace komplikovanější než u homogenních substrátů (viz výše). Při kontaktu kapaliny s textilním materiálem lze sledovat kontaktní úhel, který je však vždy nutné považovat za zdánlivý.

Při porovnávání struktury povrchů rostlin, které vykazují extrémní hydrofobitu s textiliemi, lze najít překvapivé souvislosti.

Rostliny s vysokým stupněm hydrofobity mají členitý povrch, ve kterém lze identifikovat více úrovní členitosti – povrch je členitý v každém zvětšení. Jsou zde téměř makroskopické útvary o velikostech v desítkách mikrometrů ale i mirkostruktury o rozměrech v desetinách mikrometru. Pokud rostlina potřebuje odvádět vodu, ze svého povrchu vytvoří anizotropní strukturu. Tímto způsobem rostliny dosáhnou mezních kontaktních úhlů s vodou okolo 160°.

Pokud se podíváme na textilie s dostatečným odstupem, uvědomíme si společné rysy textilií a extrémně hydrofobních rostlin. I u textilií lze nalézt několik úrovní členitosti (příze, vlákna, nerovnosti na vláknech) v rozměrech od jednotek až po stovky mikrometrů. Viz obr. 5.

Na tomto základě je založen odperlující efekt (hydrofobní úprava) textilií, kde můžeme dosáhnout kontaktních úhlů na úrovni 140°. I přes vyšší porozitu textilií nejsou tedy běžně dosahované kontaktní úhly na textiliích stejně vysoké, jako na některých rostlinách. Základním z důvodů je již zmíněný rozdíl v rozměru povrchových útvarů (na textilii jsou řádově větší než na rostlinách) a s tím související nestejnoměrnost povrchu.

Vliv drsnosti povrchu na kontaktní úhel lze obecně popsat Wenzelovou rovnicí, která platí pro neorientovanou drsnost povrchu. U textilií je povrch anizotropní z hlediska kontaktních úhlů. Nejjednodušším povrchem s podobnými vlastnostmi je povrch s rovnoběžnými rýhami v povrchu.

Pro anizotropní povrchy je třeba definovat drsnost ve dvou směrech.

Ve směru působení napětí mezi kapalinou a pevnou látkou (směr šipek) není na obr. 7 vlevo povrch drsný - je dokonale hladký. Proto v tomto směru je kontaktní úhel roven kontaktnímu úhlu na hladkém povrchu. Pro kontaktní úhel platí Youngova rovnice.

Na obrázku vpravo je ve směru působení napětí mezi kapalinou a pevnou látkou (směr šipek) povrch členitý. Pro kontaktní úhel platí Wenzelova rovnice. Dle Wenzelovy rovnice je v tomto směru kontaktní úhel extrémnější než u hladkého povrchu. Pokud je například hladký povrch nesmáčivý, pak je v tomto směru tento povrch extrémně nesmáčivý.

Na tomto základě je třeba zobecnit koeficient drsnosti podle následujícího schématu – rovnice (3). Drsnost nemusí být definována pouze jako poměr plochy reálné a makroskopické, ale může být definován i jako poměr délek mezifází – reálného a makroskopického.

$$d = S_2 / S_1 \rightarrow d = L_2 / L_1 \qquad (3)$$

d – koeficient drsnosti povrchu, poměr reálného povrchu plochy povrchu vůči zdánlivé (makroskopické) ploše povrchu, S_1 – plocha mezifází reálného, S_2 – plocha mezifází makroskopického, L_1 – reálná délka mezifází ve směru působeni povrchového napětí, L_2 – makroskopická délka mezifází ve směru působeni povrchového napětí.

Povrch tvořený paralelními vlákny je blíže textilii nežli povrch tvořený drážkami. Sledování vlivu vzdálenosti a orientace vláken v povrchu bylo provedeno na povrchu tvořeném paralelně uspořádanými vlákny. Tato struktura je matematicky lépe definovatelná a analyzovatelná než běžná tkanina, ale stále zde platí stejné zákonitosti – struktura je definovaně uspořádaná a je tvořena textilními vlákny. Vzniklá modelová struktura má výraznou anizotropii, která je zřejmá z obr. 8.

EXPERIMENTÁLNÍ ČÁST

Experimentálně byl povrch realizován navinutím vrstvy vláken paralelně v těsném kontaktu na pevnou podložku tak, aby se vlákna nekřížila a byla vzájemně rovnoběžná. K navíjení vrstvy bylo použito speciální zařízení, které umožnilo měnit stoupání návinu a počet vrstev vláken. Vlákna byla z důvodu praktičnosti použita v podobě monofilu o vyšším průměru, resp. multifilu v případě velmi jemných vláken. Průměr použitých vláken byl v rozmezí od 10 do 500 μm. Povrch vzniklé struktury byl hydrofobizován tenkou hydrofobní vrstvou na bázi perflouralkánu.

Na testovaný povrch byla nanesena kapka o objemu 20 μl (20 mm^3) pomocí mikropipety. Kapka byla snímá-

na ze dvou směrů – viz následující schéma. Následně byla k již sedící kapce přidána kapka a opět byla kapka sejmuta z obou směrů. Takto byl objem přisedlé kapky zvyšován dokud nebylo dosaženo objemu 100 µl.

Pro případ těsného kontaktu vláken je zdánlivý kontaktní úhel ve směru pozorování A až 150° pro případ, že reálný kontaktní úhel je 90° a přisedlá kapka je alespoň řádově většího rozměru než průměr vlákna. S rostoucí vzdáleností sousedních vláken roste i maximální hodnota zdánlivého kontaktního úhlu – teoreticky až k 180°. Pokud ovšem vlákna budou příliš vzdálena, pak se na nich kapalina neudrží – steče z vláken.

Pro případ těsného kontaktu vláken je zdánlivý kontaktní úhel ve směru pozorování B roven 90° pro případ, že reálný kontaktní úhel je 90°. S rostoucí vzdáleností sousedních vláken roste i hodnota zdánlivého kontaktního úhlu – teoreticky až k 180°. Pokud ovšem vlákna budou příliš vzdálena, pak se na nich kapalina neudrží – steče z vláken.

Pokud by tedy byla vytvořena soustava vláken v těsném dotyku a nanesla by se na tento povrch kapka kapaliny s reálným kontaktním úhlem 90°, pak by měl být podle výše uvedených úvah pozorován ve směru A zdánlivý kontaktní úhel až 150° a ve směru B 90°. Tento povrch byl realizován a experimentálně byl ve směru A nalezen kontaktní úhel až 140° a ve směru B asi 110°. Tyto hodnoty byly naměřeny na vláknech průměru od 10 do 500 µm. Odchylky experimentu od teorie jsou pravděpodobně dány nedodržením těsného kontaktu sousedních vláken – problémy přinášela zejména manipulace s vlákny o průměru 500 µm .

ZÁVĚR

Kontaktní úhly mezi kapalinou a textilií jsou pouze zdánlivé – jejich velikost není dána Youngovou rovnicí (rovnováhou mezipovrchových sil), ale nezanedbatelně i strukturou povrchu textilie. V práci byla velká pozornost věnována členitosti povrchu vlákenného útvaru a jejímu vlivu na kontaktní úhel textilie-kapalina-vzduch. Popis geometrie povrchu reálné textilie není k dispozici s ohledem na extrémně komplikovanou strukturu textilie a její nestejnoměrnost. Problém reálné textilie byl řešen na zjednodušeném, ale fyzikálně velmi blízkém modelu struktury tvořené těsně uspořádanými paralelními vlákny – viz obr. 10. Tento povrch je blízký textilii v mnoha ohledech: zachovává si porozitu reálné textilie, vlákna jsou součástí uspořádané struktury a vzniklá struktura je výrazně anizotropní. Takto definovaný povrch je možné i relativně snadno realizovat a experimentálně ověřit jeho chování. Experimentálně bylo zjištěno, že kontaktní úhly jsou v souladu s navrženou teorií směrově závislé a jejich velikost je v souladu s navrženým teoretickým modelem.

Teoreticky zajímavým důsledkem těchto pokusů a analýz je zjištění, že pokud jsou vlákna vzájemně vzdálenější, pak lze dosáhnout extrémnějších kontaktních úhlů. Praktickým důsledkem je zjištění, že mechanickou změnou vzdálenosti vláken v povrchu lze v relativně širokých mezích měnit hydrofobitu textilie.

AMORPHINITY (CRYSTALLINITY) OF SOME FIBER TYPES

Sodomka L., Kovačič V.

Technical University in Liberec, Czech Republic, Lubomír.sodomka@volny.cz

The paper proposes a simple roentgen diffractographic method for crystallinity and amorphinity, and their values are quantified. The degree of crystallinity and amorphinity is introduced, and an evaluation of nomex, kevlar, greystone and glass is performed.

1. Theoretical

All of the physical properties of material are dependent on their structure on a nanoscopic scale, which means the dimension of their atoms and molecules and their distribution [1, 2, 3]. From the knowledge of their structure, it is possible to estimate, deduce or forecast some properties. Any prediction concerning fibers is mostly oriented to wards their mechanical properties and the mechanical properties of textile fabrics can be predicted from these properties.

In addition, there are also the electronic properties of requested fibers, which are prepared through nanotechnology. It is advantageous, therefore, to also use nanofibers, which also have these properties.

The main methods for determining a quantitative or semiquantitative nanostructure is the application of a roentgen diffractometric structural analysis [4]. The structural determination of simple matter is relatively elementary. In a textile structure the fundamental structural component is mostly the polymer fibers, which are of a complicated structure, and it is frequently necessary to limit the degree of exactness in order to obtain some simplifyied results. In this contribution a simple diffractometric method for obtaining some structural information and an evaluation are proposed.

A great advantage of fibers is that they generally have a greater mechanical moduli and strength than arises in bulk materials. They have a more perfect structure than bulk materials do. High strength (HS) and high moduli (HM) fibers are governed through their molecular fiber structure, and their binding forces are the so-called nanostructures. The nanostructure is determined in bulk using roentgen diffraction, or in special cases through neutron diffraction, andthe structure of the surface and/or thin films are determined through electron diffraction [1–4].

Fiber nanostructures are more complicated then simple anorganic matter. Therefore, roentgen diffractograms are also more complex, and their interpretation is more complicated. Polymer fibers are partly crystallic and partly amorphous; therefore, an evaluation of diffractograms is not easy. For a rapid on-line fiber A (C) evaluation, a simple method is necessary. A simple method is proposed for the graphitization of carbon fibers and carried out [5, 6]. For determining a C, A fiber the foregoing graphitization method was improved and generalized. For the CA estimation a new degree of quantity, amorphinity (A) and crystallinity (C) D_A and D_C analogous to the degree of graphitization treated in [5], [6], was proposed. The definition of D_C is as follows

$$D_C = I(hkl)_{max}/W(hkl)_{1/2} \quad (1)$$

where the symbols $I(hkl)_{max}$ and $W(hkl)_{1/2}$ have the following meaning: $I(hkl)_{max}$ is the peak intensity of the (hkl) reflection, and $W(hkl)_{1/2}$ is the halfbreadth t.i. the diffraction lines breadth in the half altitude of the $I(hkl)_{max}$. The D_C determination is reduced to a determination of $I(hkl)_{max}$ and $W(hkl)_{1/2}$, which can be measured on the diffraction line with the reflection (Miller) index (hkl).

An elemental theory for determining the degrees of amorphinity and crystallinity D_A and D_C can now be used for determining the fiber types of two polymers and one greystone and glass ones.

The degree of amorfnity D_A is defined as

$$D_A(hkl) = W(hkl)_{1/2} / I(hkl)_{max} = 1/D_C \quad (2)$$

or can be calculated indirectly using the relation

$$D_A = 1 - D_C. \quad (3)$$

2. Experimental

The diffractometric measurements were performed using a Siemens automatic diffractometer. The prepared probes were treated through the monochromatic roentgen radiation CuK_α using the wave length λ = 0.154 nm. The whole diffraction spectra for the polymer Nomex, Kevlar , greystone and glass fibers are presented in Figs.1, 2, 3 and 4.

The straightline in Figs. 1, 2, 3, 4 separates the difraction lines from the background.

3. Evaluation of the measurements

From the diffractograms in Figs.1, 2, 3, 4, the quantities $I(hkl)_{max}$ and $W(hkl)_{1/2}$ were determined a the degrees of the fiber amorphinity and crystallinity for the

grey fibers

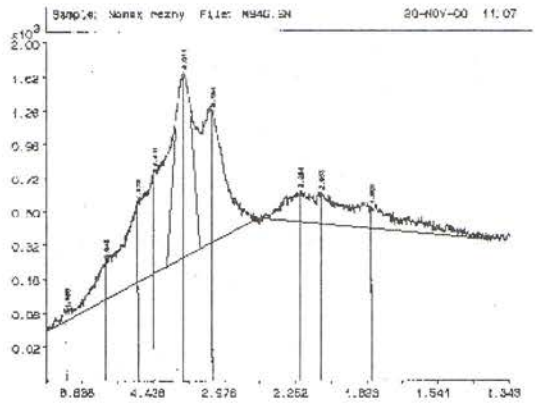

Fig. 1 Diffractogram of nomex fibers

grey fibers

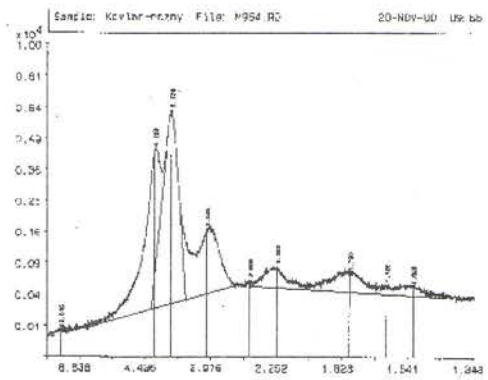

Fig. 2 Diffractogram of kevlar fibers

grey fibers

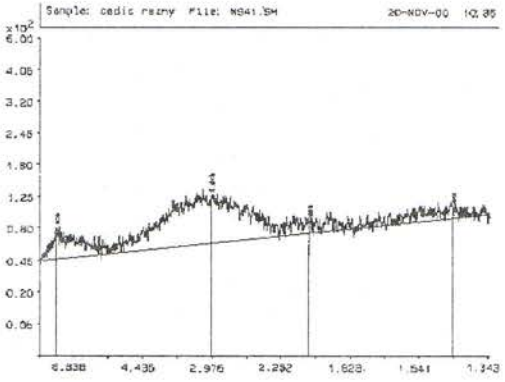

Fig.3 Diffractogram of greystone fibers

grey fibers

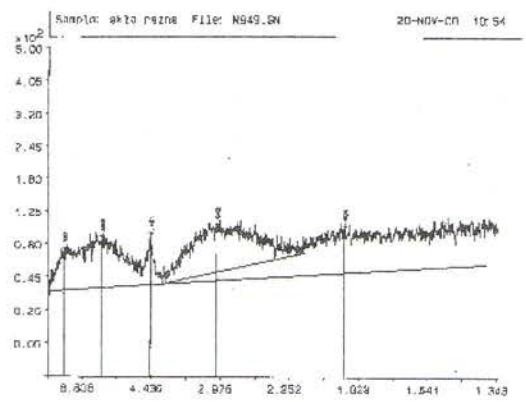

Fig.4 Diffractogram of glass fibers

Nomex, Kevlar, greystone, and glass fibers D_{AN}, D_{AK}, D_{AS}, D_{AG} (and/or D_{CN}, D_{CK}, D_{CS}, D_{CG}) were calculated. The results are summarized in table 1.

From the degree of relative amorphinity (crystallinity) D_A (D_C), the crystal ratio in the fibers can be estimated; for the Nomex fibers it is 99 (1.1) percent, for the Kevlar 94.5, (5.5) percent, the amorphous (crystal) ratio in the greystone and glass is approximately 100 percent,

Table 1 Degrees of amorphinity and crystallinity of Nomex, Kevlar, greystone and glass fibers

Quantity	Fibers			
	Nomex	Kevlar	Greystone	Glass
$I(hkl)_{max}$ (rel.u.)	41	48	8	12
$W(hkl)_{1/2}$ (rel.u.)	5	5	30	25
D_A (%)	≈ 92	90.5	99.15	99.5
D_C	≈8.0	9.5	0.25	0.48
I_{mav}	71	70	44	36
Strength in GPa	~ 28	28	2.48	E 1.75
Tensil mod. in GPa	~100	125	81	70

which in the second case can be ignored. Both of the latter fibers are in a glassy state.

The strength of the glassy fibers is caused according to the Zacheriansen-Stevels glass theory through their mesh structure or after Porai – Kosic through the clusters of nanoparticles (see [1], [2] chap.17).

All of the fibers studied have a relatively high strength and tensile modulus as is shown in Table1.

From Table 1, it can be seen that the mechanically studied fiber properties are comparable with one another, whereas the degrees of crystallinity are very different. The explanation for these facts consists in the fact that the crystal binding forces are of the same order as the forces in the glass (amorphous) network are.

The degree of amorphinity (crystallinity) is interpreted to mean that the structures differ only in their structural order.

4. Degree of the amorphinity (crystallinity) and its relation to entropy

From the foregoing text it is possible to assume that

the degree of crystallisation (D_C) is a measure for the order in the fiber structure and not for the binding forces and that D_A is a measure for the disorder in the fibers. This means that D_A (D_C) also has to cohere with the entropy S of the fibers. When the Boltzmann statistical relation between the entropy S and thermodynamic probability P is used, $S = k_B \ln P$ (see [3] chap.6) and the elemental relation between P and D_A is formulated as $P = KD_C$, where K is the proportionality factor, and k_B is the Botzmann constant; then for the entropy S, the following relation using the formulas (1) and (2) implies

$$S = k_B \ln KD_A = k_B \ln KW(hkl)_{1/2} /(I(hkl)_{max}) = \\ = k_B \ln K + k_B \ln W(hkl)_{1/2} - k_B \ln I(hkl)_{max} \quad (2)$$

From the formula it can be seen that the entropy of the fiber structure can be determined through the roentgen diffraction line profiles, which means through the quantity $W(hkl)_{1/2}$ and $I(hkl)_{max}$, which can be relatively easily reached using the difractometric measurements.

The support of the National Grant Agency of CZ No. 106-01-0387 and VC Textil FT TU in Liberec LN00B090 and 1M4674788505

5. Reference

[1] Sodomka, L.: Physics of condensed matter, I,II,III. Adhesiv Liberec 2002, 2003
[2] Sodomka, L.,Fiala, J.: Physics and chemistry of condensed matter 1,2.Adhesiv Liberec 2003, 2004
[3] Sodomka, L.: Fundamental physics for application. Adhesiv Liberec 2005 on CD
[4] Sodomka, L.: Roentgen diffractometry of solids. SNTL Prague 1960
[5] Sodomka, L.: Degree of graphitisation. Vlákna a Textil 11(2) 39-42 (2004)
[6] Sodomka, L.: Degree of graphitization. Material structure12 (2) 93 (2005)

Received: September 2005

Amorfinita (kryštalinita) niektorých typov vlákien

Translation of abstract:
Amorphinity (crystallinity) of some fiber types

V tomto príspevku je navrhnutá jednoduchá rontgenová difrakčná metóda pre kvantifikovanie kryštalinity a amorfinity. Je uvedený stupeň kryštalinity a amorfinity hodnotený u vybraných typov vlákien ako sú nomex, kevlar, greystone a sklo.

USE OF STATISTICAL APPROACH FOR IMAGE ANALYSIS OF VISUALIZED TRANSPARENT POLYMERIC FOILS

Syrová L.*, Ravas R.*, Jambrich M.**, Grman J.*

*Faculty of Electrical Engineering and Information Technology, Bratislava

**Faculty of Industrial Technologies TnU A. Dubcek, Puchov

The contribution treats the topic of processing the experimentally gained information on the properties of optically transparent polymeric foils. Schlieren optical system was used to examine and visualize refractive index distribution. Statistical approach enables useful classification of different types of polyolefine foils into classes. Experimental results and their statistical interpretation are presented as well. The successfulness of classification was verified. Signature oriented classifier on the base of neural network has been used.

INTRODUCTION

Optical visualization methods use changes in the absorption of photons during their transmission through mechanically loaded regions of transparent polymeric foils. The main advantage of these methods is that they provide information that can be used for further processing after photographic or digital recording. Of the many methods for visualizing refractive-index nonhomogeneities in transparent media, the schlieren method is one of the oldest and simplest. As an instrument, a schlieren apparatus is sensitive to transverse refractive index gradients in the test object. These gradients cause incoming light rays to undergo angular deviations, which are in turn encoded by means of selective interaction with a spatial filter, named a knife edge cutting off part of the transmitted light, e.g. an appropriate spatial filtering blocks the undeviated light while allowing the transmission of some refracted light. The camera objective focuses the test object onto the recording plane, where one receives a reduced intensity of light, depending on the amount of light cut off by the knife edge [1], [2].

IMAGE PROPERTIES

For image processing it is necessary to correct influence of light source inhomogeneity , influence of the optical string and of the sensing device for evaluation of images gained by the optical visualization of polymeric foils [3], [4]. One of the possibilities is to use reference image picked up without presence of tested object [5]. The reference image can be taken as an image of errors of the whole optical system on the assumption that we have used a virtual light source [6]. Correction of brightness errors is necessary for the further image processing by the statistical methods.

In an ideal image of visualized foils the changes of brightness reflect changes of the refractive index of test material, changes of thickness of material and presence of impurities and defects. The refractive index depends on the density of material through which light beams traverse [7].

Properties of images can be described by the histograms of relative occurrences of grey levels. The attributes of histograms can be numerical characterized using moments of distribution as the mean value of grey level

$$m = \sum_{i=1}^{L} x_i p(x_i) \tag{1}$$

and centred moments of the distribution of the k-th order

$$\mu_k(x) = \sum_{i=1}^{L} (x_i - m)^k p(x_i) \tag{2}$$

where x_i is the value of i-th grey level, $p(x_i)$ is the relative occurrence of this grey level, which can be taken as the probability of occurrence of grey level and L is the number of grey levels in the image. The regularity in structure of the foil can be described by the two-dimensional autocorrelation function. In order to quantify properties of foils images it is possible to use the grey level co-occurrence matrix [8],[9].

We can characterize it as a matrix with the elements giving the occurrence of pairs of grey level in the defined direction and distance. Such a matrix can reflect the character of image structure unlike the characteristics (1) and (2). Indices of the matrix elements correspond to the grey level of the pair. The matrix is square and symmetric to the main diagonal. The number of grey level of the pre-processed image determinates dimensions of the matrix. Owing to the discrete character of image the direction angles of pairs of pixels is quantized by the step 45°. Matrix for the distance d = 1 and the angle $\alpha = 0°$ can be expressed by

$$P(i,j,d,0) = \#\{[(k,l),(m,n)] | k = m, |l - n| = d, I(k,l) = i, I(m,n) = j\} \tag{3}$$

where (m,n) and (k,l) are coordinates of pixels separated by distance d in the horizontal direction, i, j are grey levels of such pixels, where symbol # denotes the number of elements in the set. In order to calculate characteristics from such a matrix it is more suitable to use relative occurrences (frequencies) according to (4)

$$p(i,j,d,\alpha) = \frac{P(i,j,d,\alpha)}{\sum_{i=0}^{L-1}\sum_{j=0}^{L-1} P(i,j,d,\alpha)} \quad (4)$$

In [8], [9] are some features computed from the co-occurrence matrix (4). From the suitable features we can present contrast

$$f_{\ell,d,\alpha} = \sum_{n=0}^{L-1} n^2 \left\{ \sum_{i=0}^{L-1}\sum_{j=0}^{L-1} p(i,j,d,\alpha) \right\}_{|i-j|=n} \quad (5)$$

correlation

$$f_{2,d,\alpha} = \frac{\sum_{i=0}^{L-1}\sum_{j=0}^{L-1} (ij)p(i,j,d,\alpha) - m_{x,d,\alpha}m_{y,d,\alpha}}{\sigma_{x,d,\alpha}\sigma_{y,d,\alpha}} \quad (6)$$

standard deviation

$$f_{3,d,\alpha} = \sigma_{x,d,\alpha} \quad (7)$$

where the mean values $m_{x,d,\alpha}$, $m_{y,d,\alpha}$ and the standard deviations $\sigma_{x,d,\alpha}$, $\sigma_{y,d,\alpha}$ can be computed from (8)

$$\begin{aligned} m_{x,d,\alpha} &= m_{y,d,\alpha} = \sum_{i=0}^{L-1}\sum_{j=0}^{L-1} p(i,j,d,\alpha) \\ \sigma^2_{x,d,\alpha} &= \sigma^2_{x,d,\alpha} = \sum_{j=0}^{L-1} (j - m_{x,d,\alpha})^2 \sum_{i=0}^{L-1} p(i,j,d,\alpha) \end{aligned} \quad (8)$$

uniformity of energy

$$f_{4,d,\alpha} = \sum_{i=0}^{L-1}\sum_{j=0}^{L-1} p^2(i,j,d,\alpha) \quad (9)$$

and entropy

$$f_{5,d,\alpha} = -\sum_{i=0}^{L-1}\sum_{j=0}^{L-1} p^2(i,j,d,\alpha).\log_2 p(i,j,d,\alpha) \quad (10)$$

CLASSIFICATION

Under the classification we understand procedure of decision on the assigning a foil sample to the defined class of foils or to the type of foils based on the processing of image of visualized foil structure. The tool enabling to assign a foil into classes is called the classifier. One of possibilities is to use signature oriented classifiers. Numerical features that are elements of the feature vector are defined to the specific images. The end point of feature vector is called pattern of foil. It is necessary to find such signatures that enable to cluster patterns of foils belonging to the same class and simultaneously enable to separate subspaces of patterns of foils belonging to the different classes. Then it is enough to create discrimination functions enabling to divide the signature space into the disjunctive subspaces. Each subspace will contain patterns of only one class of foils in ideal case. Such rules can be derived only in simple cases. In more complicated cases classifiers based on the principle of training such neural networks must be used.

NEURAL NETWORK CLASSIFIER

At present a very perspective solution of classification problem is neural network (NN) application. Network topology depends on the choice of input data representation. The dimension of signature vector is equal to the size of network input layer. The size of output network layer depends on the number of tested classes [12]. We chose the signature vector, which components selected characteristics calculated from histogram of relative occurrences of grey levels or from grey level co-occurrence matrix were. Neural networks have the ability of generalization and universal approximation as a result of the general approximation theorem.

For classification are usually feed-forward supervised NN used. The most popular is the multilayer perceptron (MP). MP containing one hidden layer is adequate to approximation of any arbitrary continuous function. The input space of signature vectors of images must be separable into disjunctive subspaces (clusters). Every cluster then contains signatures of the same class.

EXPERIMENTAL RESULTS

The foils images were taken on the schlieren apparatus constructed according to Dr. Bolf [5] by 5 megapixels CCD camera. Gained images were corrected by reference images. The corrected images were used for statistical characteristics calculation (1), (2).

In fig. 1.a, 1.b and 1.c are displayed the sharpened corrected images of two different samples of BOPP foil AG36 and a sample of BOPP foil AC700. From images it is seen that different foils have different characteristic features that are well observed, images of different foils can be distinguished and on the contrary images of different samples show some similarities. Figures show some regularity of stochastic character. In figures 1.a, 1.b and 1.c. are also histograms of relative occurrences of grey levels. Histogram can be characterized by the position and by the shape. Histograms of images belonging to the different samples of the same kind of foil are similar and on the contrary histograms of the different kind of foil may be characterized by some dissimilarity.

In order to experimentally verify the possibility of classification of foils characteristics from the co-occur-

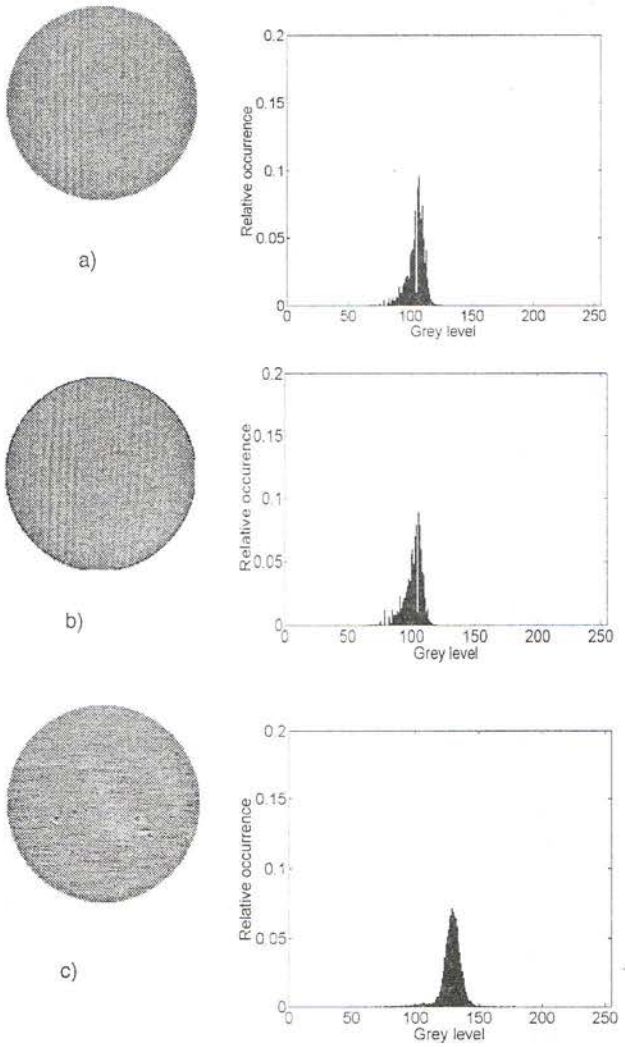

Fig.1 a) Modified image of foil AG36 with histogram, b) Modified image of an another sample of foil AG36 with histogram, c) Modified image of AC700 foil with histogram

rence matrix were calculated as well. There is 3D-representation of a section of the grey level co-occurrence matrix for two different foil samples in fig. 2.

To verify the possibilities of classification of foil images ten polyolefine foil samples from which two samples of the foil are the same, have been gained in the same condition [10]. We chose the signature vector, which components were the mean value and the centred moments of distributions of the 2nd to the 4th order .

In addition to the whole images characteristics, we have also assigned their four disjunctive parts. Fig. 3.a shows projection of signature vectors of individual classes (classes are individual types of foil) into the plane which coordinates are the mean value and the variance. Using a suitable choice of signatures there is a tendency to the grouping of patterns of individual classified classes . In fig. 3.b a detail from fig.3.a is illustrated. Selected signature vector for given groups of foils enables to create separable clusters in the space of features that fig. 3 demonstrates.

Fig. 4 exemplifies tendency to the grouping and to the separation of patterns of the same classes as used in previous case. The features were computed from the co-occurrence matrix. For the successful classification it was necessary to use signature vector containing three elements, e.g. contrast, standard deviation and correlation [11].

For experimental purposes the software system that integrates the software modules necessary to verification of arranged methods was developed. The system consists of block of image processing (fig. 5), database system, module for neural network training, block of neural network parameters saving, block of classification of foils images. The parameters of neural network were gained by network training. The software system is universal. It is possible to insert continuously foils samples that are together with the calculated statistical characteristics saved in the database into the system.

Images of seven different types of foils were used in experiments with the neural network classifier. From

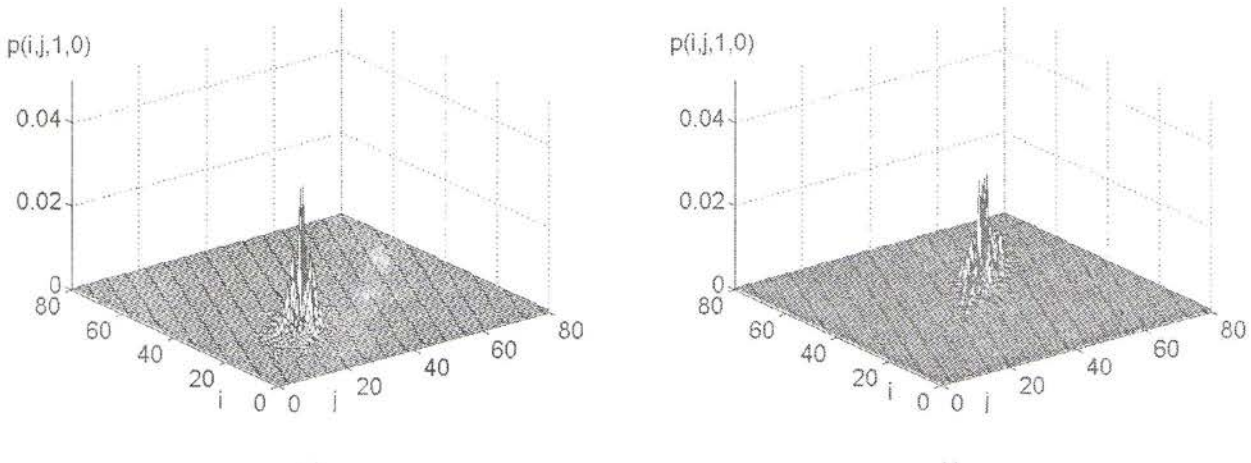

Fig. 2 3D-representation of the grey level co-occurrence matrix of foil images for d = 1 and $\alpha = 0°$ a) AG36, b) AC700

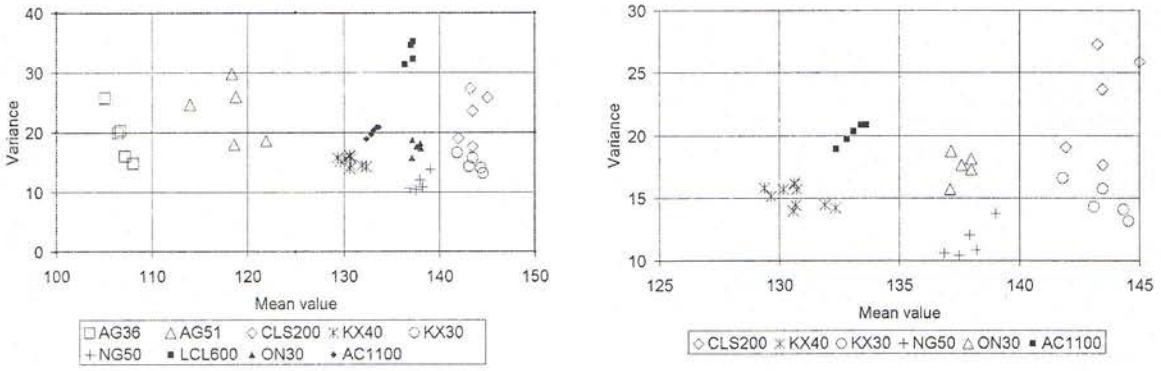

a) b)

Fig. 3 a) Projection of patterns of tested foils images to the plane mean value x variance, b) projection of patterns of tested foils images to the plane mean value x variance (part of graph from fig. 3.a)

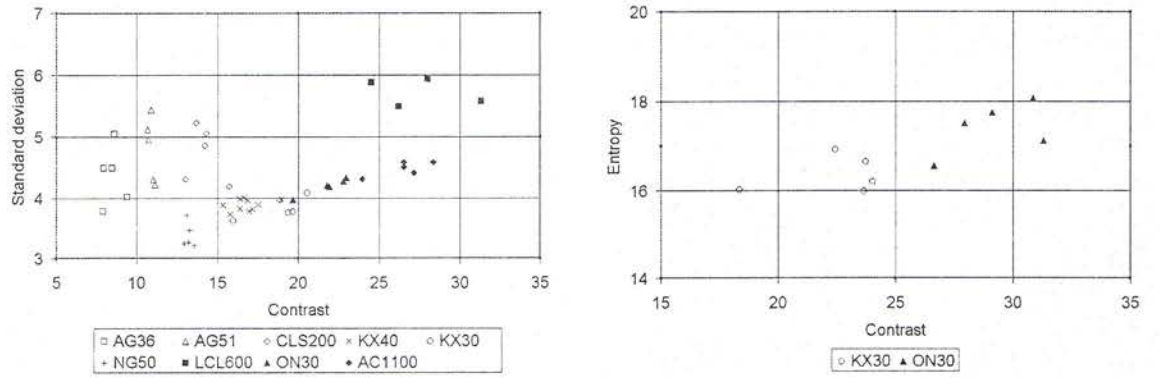

a) b)

Fig. 4 Projection of patterns of tested foils images to the plane. a) ($f_{1,1,90}$ x $f_{3,1,90}$) (contrast for d = 1 and α = 90°, standard deviation for d = 1 and α = 90°), b) ($f_{1,1,45}$ x $f_{2,1,45}$) (contrast for d = 1 and α = 45°, entropy for d = 1 and α = 45°)

each foil 16 samples were taken and stored into the database. From the database of foils samples it is possible to create different sets determined to the neural network training and the sets determined to the classifier test. The system enables to select the structure of neural network and the choice of characteristics that are elements of signature vector.

Good results were already achieved in the case of neural network training with six casually selected samples from each class. Successfulness of classification was 107 accurate classified images of 112 images. Nonsussessfulness of classification was mostly influenced by the presence of brightness fluctuation of deformations caused by defects in the foils structure. In fig. 6 the record of global error of classifier during the training in the case when foils images with defects were excluded from training and classification is presented.

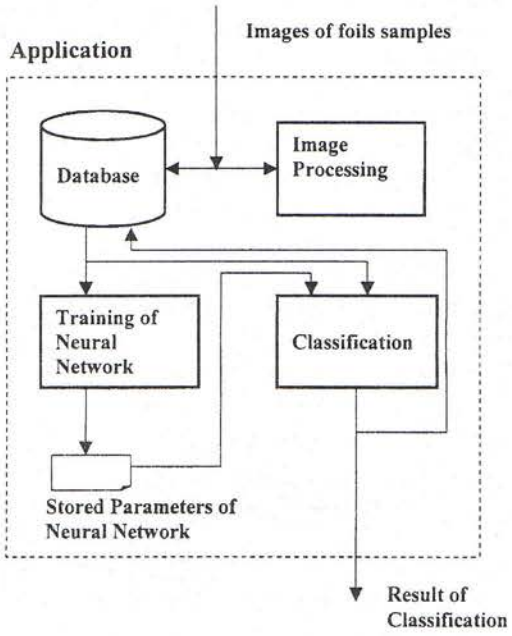

Fig. 5 Structure of software system for processing and classification of foils images

CONCLUSION

Contribution shows the possibilities of classification of visualized optically transparent polymeric foil. Statistical methods of image processing and neural network

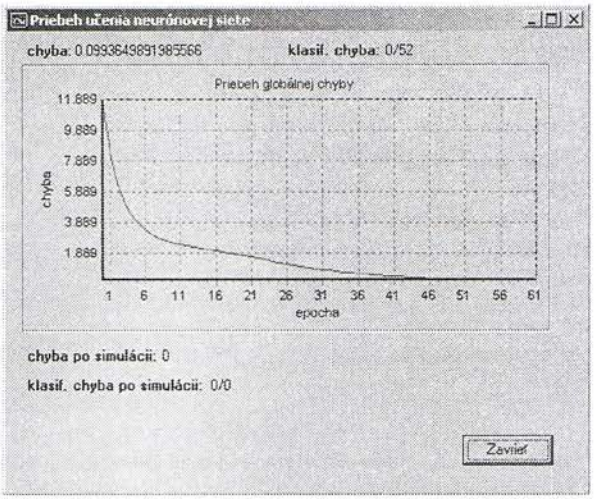

Fig. 6 Dependence of error of artificial neural network on the number of training epochs

are suitable methods enabling classification of foils. Successfulness of classification significantly depends on the quality of pictures gained on the suitable setting of schlieren apparatus and of course depends on the digital image processing. In [13] there is an interesting application of comparison pieces of polymeric foil in forensic science even if in this case only visual comparison of various pieces of the same polymeric foil without the quantitative assessment of images was used. Results published in [14] and [15] show that it is possible to apply the schlieren visualization method to the assessment of the quality of polymeric foil because it permits to locate on a pre-processed picture the places with elastic strains that are marked by variations in the level brightness (grade of level). The completion of the method with suitable statistical characteristics calculated from the pre-processed image has found the application in the field of defectoscopy, identification and classification of polymeric foils as well.

Acknowledgement: *The present work is sponsored by the research VEGA 1/0150/03 and 1/2451/05.*

REFERENCES

[1] Smith, A. J., Lim, T. T. *Flow Visualization.* London: Imperial College Press, 2000.

[2] Syrová, L., Ravas, R, Grman, J.: Principles and Application of Visualization Methods. In *Journal of Electrical Engineering*, 2001, vol. 52, no. 9–10, pp.278–283.

[3] Syrová, L.: Optical Methods for Examining and Comparing Optically Transparent Polymeric Foils. In *Journal of Electrical Engineering*, 2000, vol. 51, no. 5–6, pp. 133–137.

[4] Grman, J., Ravas, R., Syrová, L.: Use of Optical Visualization Method for Evaluation of Transparent Polymeric Foils. In: 11th International DAAAM Symposium "Intelligent Manufacturing &Automation", Opatija, 2000, pp. 167–168.

[5] Ravas, R., Syrová, L., Grman, J.: Analysis of Selected Factors in the Diagnostic Testing of Optically Transparent Polymeric Foils. In *Measurement Science Review*, 2003, vol. 3, pp. 163–167.

[6] Syrová, L., Ravas, R., Grman, J.: Use of Image Processing in the Schlieren Optical Visualization Methods. In: 12th International Scientific Conference RADIOELEKTRONIKA, Bratislava, 2002, pp. 158–161.

[7] Syrová, L., Ravas, R., Jambrich, M., Grman, J.: The Use of the Schlieren Visualization method in the Diagnostic Testing of Optically Transparent Polymeric Foils. In *Vlákna a textil*, 2004, vol. 11, no. 3, pp. 88 – 93.

[8] Haralick, R.M., Shapiro, L.G. *Computer and Robot Vision.* New York: Addison–Wesley Publishing Company, 1992.

[9] Sonka, M., Hlavac,V., Boyle, R. *Image Processing, Analysis, and Machine Vision.* Pacific Grove: Brooks/Cole Publishing Company, 1998, 770 p.

[10] Syrová, L., Ravas, R., Grman, J.: The Use of Statistical Methods for Classification of Visualized Transparent Polymeric Foils. In: 14th International DAAAM Symposium "Intelligent Manufacturing &Automation", Sarajevo, 2003, pp. 453–454.

[11] Syrová, L., Ravas. R., Grman, J.: Use of Statistical Approach for Classification of Visualized Transparent Polymeric Foils. In *Measurement Science Review*, 2003, vol. 3, pp. 139–142.

[12] LiMin, F. *Neural Networks in Computer Intelligence.* New York: McGraw-Hill Companies, 1994.

[13] Castle, D.A., Gibbins, B., Hamer, P.S.: Physical Methods for Examining and Comparing Transparent Plastic Bags and Cling Films. In *Journal of Forensic Science Society,* 1994, vol. 34, pp. 61–68.

[14] Syrová, L.: Application of Visualization Methods. In *Measurement Science Review*, 2001, vol. 1, pp. 107–110.

[15] Syrová, L., Ravas, R., Grman, J.: Use of Statistical Approach for Defectoscopy of Visualized Transparent Polymeric Foils. In *Measurement Science Review*, 2001, vol. 1, pp. 155–158.

Received: August 2005

Použitie štatistického prístupu na analýzu obrazov vizualizovaných transparentných polymérnych fólií

Translation of article:
Use of Statistical Approach for Image Analysis of Visualized Transparent Polymeric Foils

Článok je venovaný problematike spracovania experimentálne získaných informácií o vlastnostiach opticky priehľadných polymérnych fólií. Šlírov optický systém bol použitý na vizualizáciu zmien indexu lomu. Štatistický prístup umožňuje klasifikáciu rôznych typov polyolefínových fólií do tried. Experimentálne výsledky a štatistická interpretácia sú prezentované. Úspešnosť klasifikácie bola overená príznakovo orientovaným klasifikátorom na báze neurónových sietí.

ÚVOD

Optické vizualizačné metódy využívajú zmeny absorbcie fotónov počas prechodu cez mechanicky namáhané oblasti priehľadných polymérnych fólií. Hlavnou výhodou týchto metód je, že poskytujú informácie, ktoré sú použiteľné pre ďalšie spracovanie prostredníctvom fotografického alebo digitálneho záznamu. Šlírová metóda patrí k najstarším a jednoduchým metódam vizualizácie nehomogenity indexu lomu priehľadných médií. Šlírov prístroj zobrazuje priebeh gradientu indexu lomu testovaného objektu. Zmeny gradientu spôsobujú, že dopadajúci svetlený lúč sa vychyľuje zo svojej pôvodnej dráhy. Rovinné ostrie umiestnené v rovine obrazu zdroja zatieni obraz zdroja tak, že na tienidlo dopadá len časť svetla zo zdroja. V rovine ostria sa zmenia svetelné pomery a svetlo, ktoré by bolo pôvodne zachytené, môže prechádzať mimo ostria, prípadne svetlo, ktoré pôvodne prechádzalo mimo ostria, môže byť na ňom zachytené. Objektív kamery zaostruje testovaný objekt do zobrazovacej roviny, kde sa získa obraz zmien intenzity svetla, ktoré závisia od množstva svetla zachyteného na ostrí noža [1, 2].

VLASTNOSTI OBRAZU

Pre vyhodnocovanie obrazov získaných optickými vizualizačnými metódami polymérnych fólií prostriedkami číslicového spracovania obrazu je dôležité korigovať vplyv nehomogenity zdroja svetla, vplyv optickej cesty a citlivosti snímacieho zariadenia [3, 4]. Jednou z možností ich korekcie je použitie etalónového obrazu získaného snímaním obrazu bez testovaného objektu [5]. Etalónový obraz poskytuje obraz chýb celej optickej cesty zdanlivo osvetlenej ideálnym zdrojom svetla [6]. Jasová korekcia je nevyhnutná pri popise obrazu štatistickými metódami.

V ideálnom obraze vizualizovanej fólie zmeny jasových úrovní odrážajú zmeny indexu lomu testovaného materiálu, zmeny hrúbky materiálu a prítomnosť defektov a poškodenia materiálu. Index lomu závisí od hustoty materiálu, ktorým prechádza svetelný lúč [7].

Vlastnosti obrazov sa dajú popísať pomocou histogramov relatívnych početností výskytu jasových úrovní. Vlastnosti histogramov sa dajú numericky popísať pomocou momentových charakteristík ako sú stredná hodnota jasovej úrovne

$$m = \sum_{i=1}^{L} x_i p(x_i) \tag{1}$$

a centrálne momenty k-tého rádu

$$\mu_k(x) = \sum_{i=1}^{L} (x_i - m)^k p(x_i) \tag{2}$$

kde x_i je hodnota i-tej jasovej úrovne, $p(x_i)$ je relatívna početnosť tejto jasovej úrovne, ktorá môže byť považovaná za pravdepodobnosť výskytu jasovej úrovne a L je počet jasových úrovní obsiahnutých v obraze. Pravidelnosť štruktúry obrazu sa dá popísať dvojrozmernou autokorelačnou funkciou. Vlastnosti obrazov fólií je možné kvantifikovať maticou šedotónových spoluvýskytov [8, 9].

Túto maticu tvoria prvky, ktoré udávajú početnosť výskytu dvojice jasových úrovní s definovanou vzdialenosťou a smerom v obraze. Matica môže charakterizovať štruktúru obrazu na rozdiel od charakteristík (1) a (2). Indexy prvkov matice korešpondujú s hodnotami jasových úrovní dvojice pixelov v obraze. Matica je štvorcová a symetrická podľa hlavnej diagonály. Počet jasových úrovní spracovávaného obrazu určuje rozmery matice. Vzhľadom na diskrétny charakter obrazu, uhol smeru spojnice dvojice pixelov je kvantovaný s krokom 45°. Matica pre vzdialenosť d = 1 a uhol $\alpha = 0°$ sa dá definovať nasledovným vzťahom

$$P(i,j,d,0) = \#\{[(k.l),(m,n)] | k = m, |l - n| = d, l(k,l) = i, l(m,n) = j\} \tag{3}$$

kde (m,n) a (k,l) sú súradnice pixelov vzdialených o d pixelov v horizontálnom smere, i, j sú jasové úrovne týchto pixelov a symbol # znamená počet prvkov množiny, ktorá vyhovuje danej podmienke. Pre výpočet charakteristík je vhodné použiť relatívne početnosti spoluvýskytov ako je to vyjadrené vzťahom (4)

$$p(i,j,d,\alpha) = \frac{P(i,j,d,\alpha)}{\sum_{i=0}^{L-1}\sum_{j=0}^{L-1} P(i,j,d,\alpha)} \tag{4}$$

V [8], [9] sú uvedené viaceré charakteristiky počítané z matice šedotónových spoluvýskytov (4). Medzi vhodné charakteristiky patria kontrast

$$f_{i,d,\alpha} = \sum_{n=0}^{L-1} n^2 \left\{ \sum_{i=0}^{L-1} \sum_{j=0}^{L-1} p(i,j,d,\alpha) \right\}_{|i-j|=n} \quad (5)$$

korelácia

$$f_{2,d,\alpha} = \frac{\sum_{i=0}^{L-1} \sum_{j=0}^{L-1} (ij) p(i,j,d,\alpha) - m_{x,d,\alpha} m_{y,d,\alpha}}{\sigma_{x,d,\alpha} \sigma_{y,d,\alpha}} \quad (6)$$

smerodajná odchýlka

$$f_{3,d,\alpha} = \sigma_{x,d,\alpha} \quad (7)$$

kde stredné hodnoty $m_{x,d,\alpha}$, $m_{y,d,\alpha}$ a smerodajné odchýlky $\sigma_{x,d,\alpha}$, $\sigma_{y,d,\alpha}$ sa počítajú pomocou vzťahu (8)

$$m_{x,d,\alpha} = m_{y,d,\alpha} = \sum_{i=0}^{L-1} \sum_{j=0}^{L-1} p(i,j,d,\alpha)$$
$$\sigma^2_{x,d,\alpha} = \sigma^2_{x,d,\alpha} = \sum_{j=0}^{L-1} (j - m_{x,d,\alpha})^2 \sum_{i=0}^{L-1} p(i,j,d,\alpha) \quad (8)$$

rovnomernosť energie

$$f_{4,d,\alpha} = \sum_{i=0}^{L-1} \sum_{j=0}^{L-1} p^2(i,j,d,\alpha) \quad (9)$$

a entropia

$$f_{5,d,\alpha} = -\sum_{i=0}^{L-1} \sum_{j=0}^{L-1} p^2(i,j,d,\alpha) . \log_2 p(i,j,d,\alpha) \quad (10)$$

KLASIFIKÁCIA

Pod klasifkáciou fólií rozumieme proces rozhodovania o zaradení vzorky fólie k určitej skupine fólií, prípadne typu fólie na základe spracovania obrazu vizualizovanej štruktúry fólie. Na rozhodovanie zaradenia fólie do vopred definovaných tried sa používajú klasifikátory. Jednou z možností je použitie príznakovo orientovaných klasifikátorov. K daným obrazom sa definujú číselné charakteristiky – príznaky, ktoré sú zložkami príznakového vektora. Polohu koncového bodu vektora príznakov nazývame obrazom fólie. Cieľom je nájsť také príznaky, ktoré vedú k zhlukovaniu obrazov fólií prislúchajúcich tej istej triede a zároveň vedú k separácii oblastí s obrazmi fólií prislúchajúcimi do rôznych tried. Potom stačí zvoliť vhodné diskriminačné funkcie, ktorými sa dá priestor príznakov rozdeliť na disjunktné podpriestory. Každý podpriestor v ideálnom prípade bude obsahovať obrazy len jednej triedy fólií. Diskriminačné funkcie sa dajú v jednoduchých prípadoch odvodiť, v zložitejších prípadoch sa používajú klasifikátory založené na učení, ako sú napr. neurónové siete.

KLASIFIKÁTORY NA BÁZE NEURÓNOVÝCH SIETÍ

V súčasnosti sa ukazuje ako veľmi perspektívne riešenie problému klasifikácie použitie neurónových sietí. Topológia neurónových sietí závisí od výberu množiny vstupných dát. Rozmer príznakového vektora je totožný s počtom neurónov vstupnej vrstvy. Počet neurónov výstupnej vrstvy neurónovej siete závisí od počtu tried [12]. Vybrali sme príznakový vektor, ktorého zložky tvorili vybrané charakteristiky počítané z histogramu relatívnych početností jasových úrovní a z matice šedotónových spoluvýskytov. Neurónové siete majú schopnosť generalizovať a majú schopnosť nájsť riešenie obecnej aproximačnej úlohy ako dôsledok všeobecnej aproximačnej teorémy.

Pre klasifikáciu bola použitá dopredná neurónová sieť s učením. Medzi často používané patrí viacvrstvový perceptron. Obsahuje jednu skrytú vrstvu, ktorá stačí na aproximáciu ľubovoľnej spojitej funkcie. Množina vstupných príznakových vektorov má byť separovateľná do disjunktných podpriestorov (zhlukov). Každý zhluk potom obsahuje príznaky tej istej triedy.

EXPERIMENTÁNE VÝSLEDKY

Obrazy fólií boli získané šlírovým prístrojom konštruovaným Dr. Bolfom [5] a zosnímané 5 megapixelovou CCD kamerou. Nasnímané obrazy boli korigované pomocou referenčných obrazov. Korigované obrazy boli použité pre výpočet štatistických charakteristík (1), (2).

Obr.1 a) Modifikovaný obraz fólie AG36 s histogramom, b) Modifikovaný obraz inej vzorky fólie AG36 s histogramom, c) Modifikovaný obraz fólie AC700 s histogramom

Na obrázkoch 1.a, 1.b a 1.c sú zobrazené ostrené korigované obrazy dvoch rôznych vzoriek BOPP fólie AG36 a vzorka BOPP fólie AC700. Na obrázkoch je vidieť, že rôzne fólie majú rôzne pozorovateľné charakteristické črty, obrazy rôznych fólií sa dajú rozlíšiť a naopak obrazy rôznych vzoriek tej istej fólie vykazujú určité podobnosti. Na obrázkoch je vidieť určitú pravidelnosť stochastického charakteru. Na obrázkoch 1.a, 1.b a 1.c sú znázornené aj histogramy relatívnych početností výskytu jasových úrovní. Histogramy môžu byť popísané polohou a tvarom. Histogramy obrazov prislúchajúce rôznym vzorkám tej istej fólie sa podobajú a naopak histogramy rôznych druhov fólií môžu vykazovať určité odlišnosti.

Za účelom experimentálneho overenia možností klasifikácie fólií boli počítané aj charakteristiky z matice šedotónových spoluvýskytov. 3D reprezentácie výrezov matice šedotónových spoluvýskytov pre dve rôzne fólie sú uvedené na obrázku 2 .

Obr. 2 3D-reprezentácia matice šedotónových spoluvýskytov obrazov fólií pre d = 1 a $\alpha = 0°$ a) AG36, b) AC700

Aby sme verifikovali možnosti klasifikácie polyolefínových fólií, použili sme desať vzoriek, z ktorých dve vzorky prislúchali tomu istému typu fólie, pričom obrazy vzoriek boli získané za tých istých podmienok

[10]. Vytvorili sme príznakový vektor, ktorého zložky boli stredná hodnota a centrálne momenty druhého a štvrtého rádu.

Obr. 3 a) Priemet príznakových vektorov obrazov testovaných fólií do roviny stredná hodnota x smerodajná odchýlka, b) priemet príznakových vektorov obrazov testovaných fólií do roviny stredná hodnota x smerodajná odchýlka (detail z obrázku 3.a)

Okrem charakteristík počítaných pre celý obraz sme použili aj charakteristiky štyroch disjunktných častí toho istého obrazu. Na obr. 3.a je znázornený priemet príznakových vektorov jednotlivých tried (pod triedami rozumieme jednotlivé typy fólií) do roviny, ktorej súradnice tvoria stredná hodnota a smerodajná odchýlka. Vhodnosť voľby príznakov poukazuje na tendenciu zhlukovania obrazov jednotlivých tried. Na obrázku 3.b je zobrazený detail z obrázku 3.a. Z obrázku 3 je vidieť, že zvolený príznakový vektor pre danú skupinu fólií umožňuje vytvoriť separované zhluky v priestore príznakov.

Obr. 4. Priemet príznakových vektorov testovaných fólií do roviny a) ($f_{1,1,90}$ x $f_{3,1,90}$) (kontrast pre d = 1 a α = 90°, smerodajná odchýlka pre d = 1 a α = 90°), b) ($f_{1,1,45}$ x $f_{2,1,45}$) (kontrast pre d = 1 a α = 45°, entropia pre d = 1 a α = 45°)

Obrázok 4 poukazuje na tendenciu zhlukovania a separácie obrazov tých istých tried ako v predchádzajúcom prípade. Príznaky boli počítané z matice šedotónových spoluvýskytov. Pre úspešnosť klasifikácie je potrebné použiť v tomto prípade príznakový vektor s tromi zložkami, napr. kontrast, smerodajná odchýlka a korelácia [11].

Obr. 5 Štruktúra programového systému na spracovanie a klasifikáciu obrazov fólií

Na realizáciu experimentov bol vyvinutý programový systém integrujúci programové moduly na verifikáciu použitých metód. Systém pozostáva z blokov (obr. 5) ako je blok spracovania obrazu, databázový modul, modul na trénovanie neurónovej siete, blok na ukladanie parametrov neurónovej siete a blok klasifikácie obrazov fólií. Parametre neurónovej siete sa získavajú trénovaním siete. Programový systém je otvorený. Umožňuje priebežne vkladať obrazy vzoriek fólií spolu s počítanými štatistickými charakteristikami do databázy.

Obrazy siedmich rôznych typov fólií boli použité v experimentoch s klasifikátorom na báze neurónovej siete. Z databázy obrazov vzoriek fólií je možné vytvárať rôzne množiny určené na trénovanie neurónovej siete a množiny určené na testovanie klasifikátora. Systém umožňuje vyberať štruktúru neurónovej siete a vyberať charakteristiky, ktoré tvoria zložky príznakového vektora.

Obr. 6 Grafický záznam procesu trénovania umelej neurónovej siete

Dobré výsledky sa dosiahli už po natrénovaní neurónovej siete použitím šiestich vzoriek z každej triedy. Dosiahnutá úspešnosť klasifikácie bola 107 správne klasifikovaných vzoriek zo 112 obrazov. Neúspešnosť klasifikácie bola spôsobená hlavne prítomnosťou jasových zmien a deformácií v dôsledku prítomnosti defektov v štruktúre fólie. Na obrázku 6 je znázornený priebeh globálnej chyby klasifikácie počas tréningu pre prípad, keď obrazy fólií obsahujúce defekty boli vyradené z trénovania a klasifikácie.

ZÁVER

Príspevok poukazuje na možnosť klasifikácie vizualizovaných opticky priehľadných polymérnych fólií. Štatistické metódy používané pri číslicovom spracovaní obrazu sú vhodnými metódami umožňujúcimi klasifikovať obrazy fólií. Úspešnosť klasifikácie významne závisí od kvality získaných obrazov, od vhodného nastavenia šlírovho prístroja a samozrejme od číslicového spracovania obrazu. V [13] je publikovaná zaujímavá aplikácia porovnávania častí polymérnych fólií v kriminalistike, v tomto prípade sa použilo len vizuálne porovnávanie rôznych častí tej istej fólie bez kvantitatívneho vyhodnotenia ich obrazov. Výsledky publikované v [14] a [15] poukazujú na možnosť použitia šlírovej vizualizačnej metódy na vyhodnotenie kvality polymérnych fólií, pretože umožňujú detekovať na predspracovaných obrazoch miesta s deformáciami, ktoré sa vyznačujú výraznými zmenami jasových úrovní. Doplnenie metódy vhodnými štatistickými charakteristikami počítanými z predspracovaných obrazov môžu nájsť uplatnenie v oblasti defektoskopie, identifikácie a klasifikácie polymérnych fólií.